

Lodz University of Technology

SCIENTIFIC BULLETIN

PHYSICS

Vol. 38

LODZ 2017

LODZ UNIVERSITY OF TECHNOLOGY

SCIENTIFIC BULLETIN

No. 1219

PHYSICS

Vol. 38

LODZ 2017

ZESZYTY NAUKOWE POLITECHNIKI ŁÓDZKIEJ
SCIENTIFIC BULLETIN OF THE LODZ UNIVERSITY OF TECHNOLOGY
BULLETIN SCIENTIFIQUE
DE L'UNIVERSITÉ POLYTECHNIQUE DE LODZ
НАУЧНЫЕ ЗАПИСКИ
ЛОДЗИНСКОГО ПОЛИТЕХНИЧЕСКОГО УНИВЕРСИТЕТА
WISSENSCHAFTLICHE HEFTE
DER TECHNISCHEN UNIVERSITÄT IN LODZ

Editor of series: **Assoc. Professor Grzegorz Derfel, Ph.D., D.Sc.**
Subject Editor of series: **Assoc. Professor Jolanta Prywer, Ph.D., D.Sc.**

Printed version of the journal is the main version.

© Copyright by Politechnika Łódzka 2017

Adres Redakcji – Адрес Редакции – Editor's Office
Adresse de Redaction – Schriftleitungsadresse:

WYDAWNICTWO POLITECHNIKI ŁÓDZKIEJ

90-924 Łódź, ul. Wólczańska 223
tel. 42-631-20-87, fax 42-631-25-38
e-mail: zamowienia@info.p.lodz.pl
www.wydawnictwa.p.lodz.pl

ISSN 1505-1013
e-ISSN 2449-982X

doi:10.34658/physics.2017.38
<https://doi.org/10.34658/physics.2017.38>

<http://cybra.lodz.pl/publication/3923>

Nakład 70 egz. Ark. druk. 5,0. Papier offset. 80 g 70 x 100
Wykonano w Drukarni Quick-Druk, 90-562 Łódź, ul. Łąkowa 11

CONTENTS

Mariola Buczkowska, Grzegorz Derfel – Influence of tilted surface alignment on flexoelectric domains in twisted nematic layers	5-10
Marek Izdebski, Rafał Ledzion – Verification of one-dimensional models describing anisotropy of step growth.....	11-26
Sylwester Kania, Barbara Kościelniak-Mucha, Janusz Kuliński, Piotr Słoma, Krzysztof Wojciechowski – The effect of the dipole moment on hole conductivity of polycrystalline films of two anthracene derivatives.....	27-36
Sylwester Kania, Janusz Kuliński, Dominik Sikorski – Comparative study of the influence of the reorganization energy on the hole transport of two four-cyclic arenes	37-44
Sylwester Kania, Barbara Kościelniak-Mucha, Janusz Kuliński, Piotr Słoma, Krzysztof Wojciechowski – Sensitivity of tetracene layer as an effect of entanglement.....	45-51
Paulina Komar, Patrycja Śpiewak, Marcin Gębski, James A. Lott, Michał Wasiak – Current dependence of resistances and capacitances in a vertical-cavity surface-emitting laser.....	53-60
Magdalena Marciniak, Marcin Gębski, Maciej Dems, Tomasz Czyszanowski – Subwavelength high contrast gratings as optical sensing elements.....	61-70
Marta Więckowska, Maciej Dems, Tomasz Czyszanowski – Comparison of methods for simulation of the optical properties of VCSEls.....	71-80

MARIOLA BUCZKOWSKA, GRZEGORZ DERFEL

Institute of Physics, Lodz University of Technology, ul. Wólczańska 219,
90-924 Łódź, Poland, e-mail: mbuczko@p.lodz.pl

INFLUENCE OF TILTED SURFACE ALIGNMENT ON FLEXOELECTRIC DOMAINS IN TWISTED NEMATIC LAYERS

The small deformations induced by electric field in twisted flexoelectric nematic layers were simulated numerically. The one-dimensional (i.e. homogeneous over the whole area of the layer) and two-dimensional (i.e. spatially periodic flexoelectric domains) deformations were considered. It was shown that the periodic deformations do not arise if sufficiently high pretilt angle is imposed by the boundary conditions. The value of pretilt angle necessary for elimination of domains increases with the flexoelectric coefficient e_{33} . This result is of practical meaning because the flexoelectric domains are undesirable from an applicative point of view since they destroy the homogeneous appearance of the area of an excited pixel of a display.

Keywords: nematics; flexoelectricity; director deformations; periodic patterns.

1. INTRODUCTION

Nematic liquid crystal layers confined between plane-parallel electrodes are fundamental for applications in liquid crystal devices [1]. The principle of operation of these devices is based on electrically induced deformations of director field. The deformations arise due to torques of dielectric and flexoelectric nature [2]. They can be one-dimensional or two-dimensional. In the former case the director orientation depends on the coordinate z perpendicular to the layer plane only. In the latter case, the director orientation depends on z and varies periodically along another direction parallel to the layer. As a result, the deformation is spatially periodic and is visible in the form of parallel stripes called domains [3-5]. The two-dimensional deformations are particularly favoured if nematic possesses significant flexoelectric properties which was

demonstrated in our earlier article [6]. Nematic exhibiting strong flexoelectricity adopted enhanced interest after they were discovered among substances composed of molecules with bent core [7, 8]. The flexoelectric domains are not desirable from applicative point of view since they disturb the uniform appearance of an excited pixel of a device. However, in our previous article [9] we showed that they can be avoided if the boundary conditions ensure sufficiently large surface pretilt of easy axes which determine orientation of director adjacent to the electrodes.

In the present paper we continue the calculations taking into account the nematics which exhibit parameters characteristic for the mixtures of substances composed of calamitic and bent-core molecules.

2. PARAMETERS AND METHOD

The nematic layers of thickness $d = 5 \mu\text{m}$, confined between electrodes parallel to the xy plane of the coordinate system and positioned at $z = \pm d/2$, were considered. The voltage U was applied between them. The director orientation in the layer, $\mathbf{n}(y, z)$, was determined by means of the polar angle $\theta(y, z)$ measured between \mathbf{n} and the xy plane and by the azimuthal angle $\phi(y, z)$ between the x axis and the projection of \mathbf{n} on the xy plane. Boundary conditions were given by the polar and azimuthal angles θ_{s1} , θ_{s2} , ϕ_{s1} and ϕ_{s2} which determined orientation of the easy axes \mathbf{e}_1 and \mathbf{e}_2 on the lower and upper electrode, respectively. The surface pretilt angles $\theta_{s1} = \theta_{s2}$, in the following denoted by δ , ranging between 0° and 30° , were imposed. The twist angle $\Phi = \phi_{s2} - \phi_{s1} = 90^\circ$ ensured the right-hand twist in the twisted layers. The calculations were performed for two kinds of mixtures denoted in the following as mixtures A and mixtures B. The bent-core nematics have peculiar elastic properties manifested by the specific relation between elastic constants: $k_{11} > k_{33} > k_{22}$ [10]. For this reason we adopted elastic constants ratios which differ from those found for typical calamitic nematics. The parameters of the corresponding layers are gathered in Table 1.

Table 1

The parameters of the layers

	mixtures A	mixtures B
splay elastic constants	$k_{11} = 8 \cdot 10^{-12} \text{ N}$	$k_{11} = 7 \cdot 10^{-12} \text{ N}$
twist elastic constants	$k_{22} = 3 \cdot 10^{-12} \text{ N}$	$k_{22} = 2 \cdot 10^{-12} \text{ N}$
bend elastic constants	$k_{33} = 10 \cdot 10^{-12} \text{ N}$	$k_{33} = 7 \cdot 10^{-12} \text{ N}$
dielectric anisotropy	$\Delta\epsilon = 2$	$\Delta\epsilon = 2$
bend flexoelectric coefficient	$0 - 50 \cdot 10^{-12} \text{ C/m}$	$0 - 50 \cdot 10^{-12} \text{ C/m}$
polar anchoring strength	$W_{\theta 1} = W_{\theta 2} = 10^{-4} \text{ J/m}^2$	$W_{\theta 1} = W_{\theta 2} = 10^{-4} \text{ J/m}^2$
azimuthal anchoring strength	$W_{\phi 1} = W_{\phi 2} = 10^{-5} \text{ J/m}^2$	$W_{\phi 1} = W_{\phi 2} = 10^{-5} \text{ J/m}^2$

The splay flexoelectric coefficient e_{11} was assumed to be zero since the role of the bend flexoelectric coefficient e_{33} is predominant in bent-core materials. Its value was varied between 0 and 50 pC/m. The saddle-splay elastic constant k_{24} was assumed to be zero. The small dielectric anisotropy of the mixtures was adopted according to small positive or negative values measured for the bent-core nematics. Such small dielectric anisotropy only slightly influenced the effects of flexoelectric nature which were our main interest.

We simulated both the small one-dimensional deformations as well as the small periodic deformations after application of voltage. The director distribution along the z axis was found in the former case and the distribution in the cross-section of a single stripe was determined in the latter case. The method of computations was comprehensively described in our previous paper [9]. The equilibrium director distribution was found by minimisation of free energy per unit area of the layer at the bias voltage which caused small deformation. The state of minimum energy was obtained in the course of an iteration process. During a single cycle of computations, the variables describing the director distribution were varied successively by small intervals. The free energy per unit area of the layer was calculated after each change. If the new energy was lower than the previous one, the changed values of the variables were accepted. In the opposite case, the variables remained unchanged and another attempt was made. The cycles were repeated until further reduction in the total free energy could be neglected. The energies per unit area of the layer calculated for one-dimensional and two-dimensional deformations arising at the same voltage were compared. The state with lower energy was chosen as the one which is realized. The calculations were performed for increasing voltages starting from $U = 0$. The threshold voltage for the periodic deformations, U_c , was determined as the voltage at which the energy of them became smaller than that for homogeneous deformations.

2. RESULTS

In the case of layers with zero pretilt, the spatially periodic deformations arose when the threshold voltage U_0 was exceeded. The layers with non-zero pretilt started to deform homogeneously already from $U = 0$. The two-dimensional deformations appeared at the threshold voltage U_c on the background of the small homogeneous deformation. The threshold voltage decreased with increasing flexoelectric coefficient e_{33} . For given value of e_{33} the threshold increased when the pretilt angle was enhanced. Both dependences are presented for the mixtures A and B in Figs. 1 and 2 respectively, where thresholds U_c are plotted as functions of pretilt angle δ for several values of e_{33} .

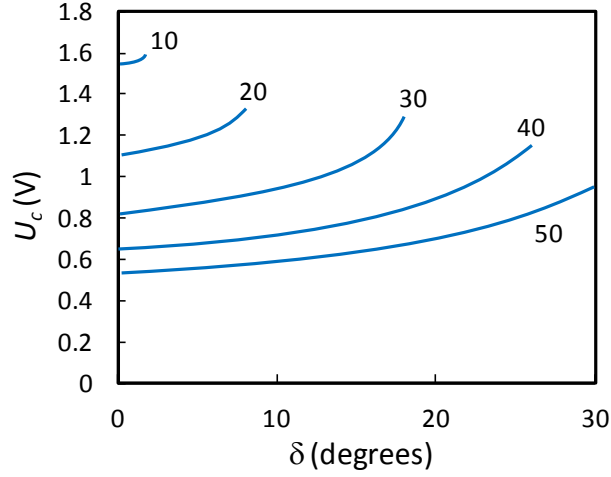


Fig. 1. Threshold voltage U_c as a function of surface pretilt angle δ for mixtures A. Values of flexoelectric coefficients e_{33} (in pC/m) are indicated at the curves

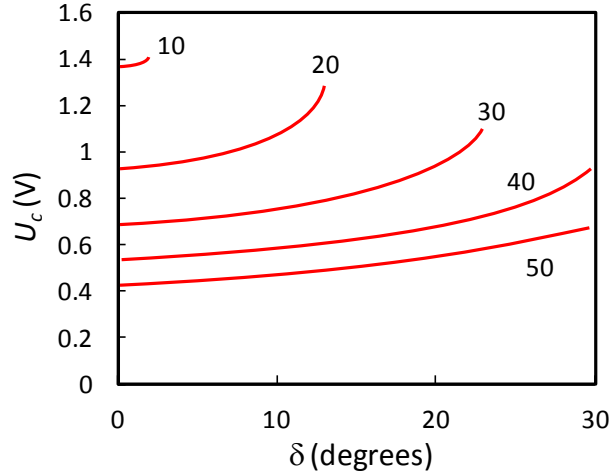


Fig. 2. Threshold voltage U_c as a function of surface pretilt angle δ for mixtures B. Values of flexoelectric coefficients e_{33} (in pC/m) are indicated at the curves

It is evident that for the weakly flexoelectric nematics there exist some critical pretilt angles δ_c above which the periodic deformations are no more energetically favoured therefore they do not occur. This means that the

flexoelectric domains are eliminated. In the case of strongly flexoelectric mixture the critical pretilt exceeds 30° . However we restricted our calculations to this value since larger pretilt angles seem to be impractical.

The results are summarised in Fig. 3. they are coherent with those reported in [9]. The plots of the critical pretilt angle as a function of flexoelectric coefficient limit the set of parameters δ and e_{33} for which the flexoelectric domains are favoured from the set for which the domains are eliminated.

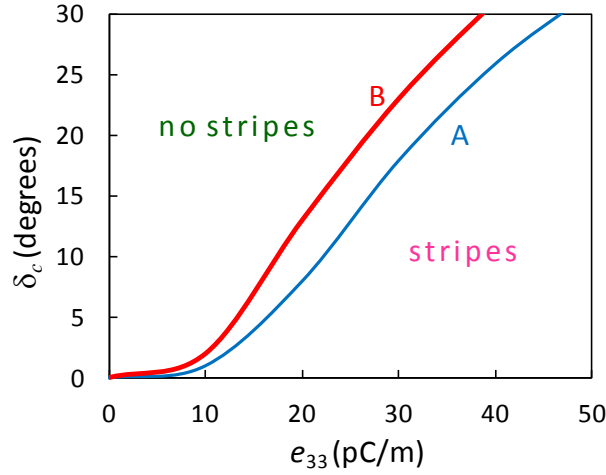


Fig. 3. Limiting pretilt angle δ_c as a function of flexoelectric coefficient e_{33} for mixtures A and B

The results of this work show that the sufficiently large surface pretilt angle allows to avoid the flexoelectric domains when the nematic material possesses strong flexoelectric properties.

REFERENCES

- [1] Yang D.K., Wu S.T. 2006. Fundamentals of liquid crystal devices. New York (NY): John Wiley & Sons Inc.
- [2] Blinov L.M. 2011. Structure and Properties of Liquid Crystals. New York (NY): Springer.
- [3] Vistin L.K. 1970. Electrostructural effect and optical properties of a certain class of liquid crystals. *Sov Phys Crystallogr.*15:514–515.
- [4] Umanski B.A., Chigrinov V.G., Blinov L.M., Podyachev Y.B. 1981. Flexoelectric effect in twisted liquid-crystal structures. *Sov Phys JETP.*54:694–699.

- [5] Chigrinov V.G., Belyaev V.V., Belyaev S.V., Grebenkin M.F. 1979. Instability of cholesteric liquid crystals in an electric field. *Sov Phys JETP*. 50:994–999.
- [6] Buczkowska M., Derfel G. 2017. Spatially periodic deformations in planar and twisted flexoelectric nematic layers. *Phys Rev E*. 95:062705.
- [7] Harden J., Mbanga B., Éber N., et al. 2006. Giant flexoelectricity of bent-core nematic liquid crystals. *Phys Rev Lett*. 97:157802.
- [8] Jáklí A. 2013. Liquid crystals of the twenty-first century – nematic phase of bent-core molecules. *Liq Cryst Rev*. 1:65–82.
- [9] Buczkowska M., Derfel G. 2017. Influence of the surface pretilt angle on spatially periodic deformations in nematic layers. *Liq Cryst*. DOI:10.1080/02678292.2017.1402097.
- [10] Kaur S. 2016. Elastic properties of bent-core nematic liquid crystals: the role of the bend angle. *Liq Cryst*. 43: 2277-2284.

WPLYW UKOŚNEGO UPORZĄDKOWANIA POWIERZCHOWEGO NA DOMENY FLEKSOELEKTRYCZNE W SKRĘCONYCH WARSTWACH NEMATYKA

Streszczenie

Niewielkie odkształcenia wywołane polem elektrycznym w warstwach skręconego nematyka były symulowane numerycznie. Badano odkształcenia jednowymiarowe (tj. jednorodne na całej powierzchni warstwy) i dwuwymiarowe (tj. przestrzennie okresowe). Wykazano, że odkształcenia okresowe nie powstają, gdy warunki brzegowe narzucają odpowiednio duży kąt nachylenia uporządkowania powierzchniowego. Jego wartość rośnie ze wzrostem współczynnika fleksoelektrycznego e_{33} . Wynik ten ma znaczenie praktyczne, ponieważ występowanie domen fleksoelektrycznych w urządzeniach ciekłokrystalicznych jest niepożądane.

MAREK IZDEBSKI, RAFAŁ LEDZION

Institute of Physics, Lodz University of Technology, ul. Wólczańska 219,
90-924 Łódź, Poland, e-mail: marek.izdebski@p.lodz.pl

VERIFICATION OF ONE-DIMENSIONAL MODELS DESCRIBING ANISOTROPY OF STEP GROWTH

Models that allow to obtain directional dependencies of normal velocity of a straight step on the (001) face of Kossel crystal and its edge free energy are reviewed. The dependencies were considered in a wide range of crystal growth conditions, which showed some significant discrepancies between the models and limitations in the scope of their applicability. The results presented concern on one-dimensional kinetic and thermodynamic models of a single step.

Keywords: step growth, Burton Cabrera Frank theory, Monte Carlo simulation of crystal growth.

1. INTRODUCTION

The growth of a perfect crystal is possible only when nuclei of critical size are forming on its surface. However, the rate of creation of critical nuclei, which can be estimated on thermodynamical basis, is too small to explain many experimental data on the growth rate. This observation led Frank to formulate suggestions that those crystals which grow are not perfect and the steps on the crystal surface are generated by dislocations [1]. Therefore, a need arose to develop theoretical models predicting the structure of the step, its edge free energy, velocity of motion and their directional dependencies. Among the published works, the theory developed by Burton, Cabrera and Frank (BCF) in 1959 [2] is particularly well known and is still cited in recent papers. While the BCF theory is based on thermodynamic grounds, a kinetic approach has been applied in some other works. The latter include mainly analytical approach based on a stationary kinetic equation method [3-5] and some fragmentary results obtained using of one-dimensional (1D) Monte Carlo (MC) simulations [6] and two-dimensional (2D) MC simulations [7-9]. Although many other works on crystal growth are known from the literature, most of them do not provide any quantitative description of anisotropy of step growth.

The motion and interaction of the spirals generated by different dislocations significantly affect the kinetics of crystal growth. However, available quantitative analyzes of this effect are still focused on a particularly simple case of isotropic spirals [10-14]. In the anisotropic case, an equation describing time evolution of any contour may be formulated as in Ref. [15] based on the Ginzburg-Landau theory

$$\frac{\partial \xi}{\partial t} = -D(\theta) \left[\left(\gamma(\theta) + \frac{d^2 \gamma}{d\theta^2} \right) \frac{1}{R} - \Omega^{-1} \Delta \mu \right], \quad (1)$$

where ξ is the local displacement of the contour in the normal direction \mathbf{n} , D is a transport coefficient, θ is the angle between \mathbf{n} and any fixed vector in the system, R is the local radius of curvature of the contour, Ω is the area covered by a single growth unit, and $\gamma \Omega^{1/2} = F$ is the edge free energy per unit length of the contour. As can be seen from Eq. (1) the coefficient D is proportional to the normal velocity V of straight step. In the isotropic case Eq. (1) reduces to the form known the BCF theory $d\xi/dt = V(1 - R_c/R)$, where R_c is the critical radius. For the anisotropic motion, the directional dependencies $D(\theta)$ and $F(\theta)$ must be known from other models.

The aim of this work is to review the directional dependencies $D(\theta)$ and $F(\theta)$ resulting from models known from the literature, critical analysis of results obtained in a wide range of parameters characterizing crystal growth conditions and drawing some conclusions. Due to the wide range of necessary analyzes, we will focus in this work on 1D models. Although the 1D one-dimensional approach is relatively old, it still remains the only one for which a completely analytic derivation of the $D(\theta)$ and $F(\theta)$ dependencies is known from literature.

2. THEORY

All the works that concern one-dimensional models use some common assumptions to simplify description of a microscopic state of a step. First of all, only the (001) face of Kossel crystal is considered. Moreover, the assumption known as "solid-on-solid" is applied for two perpendicular crystallographic directions, which allows one to describe the state of a step by 1D array $h(x)$ containing the heights of columns of solid blocks in monoatomic layer (Fig. 1). This restriction excludes overhangs in a step, and limits all possible processes to locations lying on the edge of the step. The difference of columns heights at the two neighbouring locations $h(x+1) - h(x)$ determines the height of kink k , which may take any integer values $0, \pm 1, \pm 2, \dots$ measured in lattice constant units.

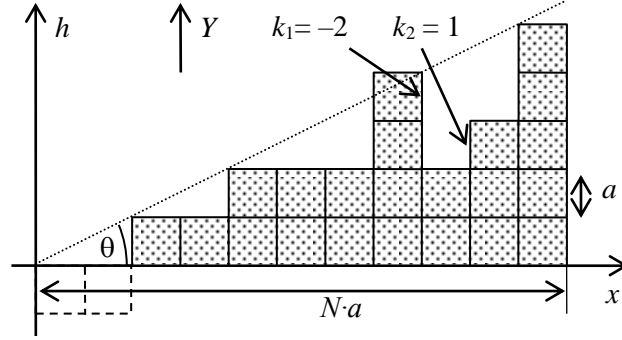


Fig. 1. The growth step on the (001) face of Kossel crystal considered as a columns of solid blocks in monoatomic layers

Let $X(k)$ be the probability of finding a kink of height k . The probability of finding any kink is

$$\sum_{k=-\infty}^{+\infty} X(k) = 1. \quad (2)$$

Following the works [2,5], the average orientation of the step will be described by the parameter h

$$h = \tan \theta = \langle k \rangle = \sum_{k=-\infty}^{+\infty} k X(k). \quad (3)$$

where θ is the angle between the step and the $+x$ crystallographic axis (Fig. 1).

Correlation between kinks at neighbouring locations leads to a system of equations, which has not been solved analytically. Therefore, the correlation was neglected in analytical works, including both the BCF theory and the works based on kinetic equations. Hence, the approximate value of the probability $X(k_1, k_2, \dots)$ of finding a given combination of neighbouring kinks [2, 4, 5] is

$$X(k_1, k_2, \dots) \approx X(k_1)X(k_2)\dots \quad (4)$$

The correlation may be, however, examined by MC simulations.

Further derivations of probabilities $X(k)$ are different in the BCF theory and in the approach based on kinetic equation.

2.1. BCF model

The paper published by Burton, Cabrera and Frank [2] refers to a number of 2D and 3D concepts, such as two-dimensional nucleation and growth pyramids. In this work, however, we refer only to that part of the paper where the problem of the structure of a step is a 1D problem.

In the BCF theory, particular processes between some selected configurations of kinks in equilibrium have been considered (a detailed description of the processes taken into account can be found in Appendix C of Ref. [2]). If the energies of the two configurations are the same, the probabilities of their occurrence are equal $X(k_1, k_2, \dots) = X(k'_1, k'_2, \dots)$. When the energy ϕ_{ss} of solid nearest neighbours interaction must be supplied in going from (k_1, k_2, \dots) to (k'_1, k'_2, \dots) configuration, the probabilities satisfy the following relationship

$$X(k'_1, k'_2, \dots) = X(k_1, k_2, \dots) \eta^2. \quad (5)$$

The term η in Eq. (5) is defined as

$$\eta = \exp(-\phi_{ss}/2k_B T), \quad (6a)$$

where k_B is the Boltzmann constant and T is temperature. In the original formulation of the BCF theory, only the energy ϕ_{ss} of solid-solid bonds is taken into account. Following thermodynamic models of Jackson [16,17] and Temkin [18] as well as kinetic models [5,6,19-21], we will also include the energies ϕ_{ff} and ϕ_{sf} of fluid-fluid and solid-fluid bonds. Each process considered in BCF, which leads to a change in the configuration of atoms without changing the number of atoms forming a crystal, is associated with a change in the energy by a certain multiple of factor $\alpha/2$. Equation (6a) can therefore be generalized as

$$\eta = \exp(-\alpha/4), \quad (6b)$$

where α is the Jackson-Temkin parameter

$$\alpha = (2\phi_{ss} + 2\phi_{ff} - 4\phi_{sf})/k_B T. \quad (7)$$

It can be proved from equations (2)-(5) that the following relations must be satisfied [2]

$$X(k) = \begin{cases} X(0)g_-^{-k}, & \text{for } k < 0, \\ X(0)g_+^k, & \text{for } k \geq 0, \end{cases} \quad (8)$$

where $0 \leq g_{\pm} \leq 1$ and

$$g_+ g_- = \eta^2, \quad (9)$$

$$X(0) = \left[1 + \eta^2 - \sqrt{(1 + \eta^2)^2 - (1 - \eta^2)^2 (1 - h^2)} \right] / (1 - \eta^2)(1 - h^2), \quad (10)$$

$$2g_+ = 1 + \eta^2 - X(0)(1 - \eta^2)(1 - h), \quad (11)$$

$$2g_- = 1 + \eta^2 - X(0)(1 - \eta^2)(1 + h). \quad (12)$$

The dependence of the normal velocity of a straight step on its direction $V(h)$ has not been proposed in the original formulation of the BCF model. Following the argumentation presented *e.g.* in Refs. [15, 22], crystal growth

occurs primarily by the absorption of atoms at kinks. Consequently, the transport coefficient D and the normal velocity V are proportional to the density of kinks C

$$D(h) \sim V(h) \sim C = [1 - X(0)](1 + h^2)^{-1/2}, \quad (13)$$

where $[1 - X(0)]$ is the density along the $[1,0,0]$ direction and the term $(1 + h^2)^{-1/2} = \cos\theta$ allows to obtain the density per unit length of the step.

In the BCF theory the configurational free energy per unit length of a straight step was found as $F = (U - TS)(1 + h^2)^{-1/2}/N$. The internal energy of the step is $U = (N + \Delta N_{\text{SF}})\alpha k_B T/4$, where $N\alpha k_B T/4$ is the energy of a perfectly

straight step and $\Delta N_{\text{SF}} = N \sum_{k=-\infty}^{+\infty} |k| X(k)$ is the increase in the number of

solid-fluid bonds due to the formation of kinks. The entropy S is given by the Boltzmann formula $S = k_B \ln W$, where W is the number of ways in which $[1 - X(0)]N$ kinks of any height can be arranged in N locations. In this calculation $X(k)N$ kinks of a given height k are treated as undistinguishable, while the kinks of different heights are distinguishable. This reasoning together with equations (2), (3) and (8) allows us to derive the formula

$$F = k_B T \left\{ \left[1 + \frac{X(0)g_-}{(1-g_-)^2} + \frac{X(0)g_+}{(1-g_+)^2} \right] \frac{\alpha}{4} + \left[\ln X(0) + \frac{X(0)g_- \ln(g_+g_-)}{(1-g_-)^2} + h \ln g_+ \right] \right\} (1 + h^2)^{-1/2}. \quad (14)$$

The approach based on the kinetic equation (which is discussed in section 2.2) may lead to other values of (g_+g_-) , $X(0)$, g_+ , g_- than those given by Eqs. (9)-(12) but the formula (14) still remains correct. In the particular case when the solution (9) can also be used, the formula (14) simplifies to the form known from the original formulation of the BCF theory [2]

$$F = k_B T \left\{ (1+h)\alpha/4 + [\ln X(0) + h \ln g_+] \right\} (1 + h^2)^{-1/2}. \quad (15)$$

2.2. Kinetic analytical approach

In the kinetic approach, the rates $dX(k)/dt$ are associated with fluxes of molecules being created and annihilated at the edge of the step. In particular, where diffusional processes are neglected and approximation (4) is applied we get the following equality for a stationary state [5]

$$\frac{dX(k)}{dt} = U_R(k+1)X(k+1) + V_R(k-1)X(k-1) - [U_R(k) + V_R(k)]X(k) = 0, \quad (16)$$

where

$$U_R(k) = \sum_{k_1=-\infty}^{+\infty} [v^+(k_1, k) + v^-(k, k_1)] X(k_1), \quad (17)$$

$$V_R(k) = \sum_{k_1=-\infty}^{+\infty} [v^+(k, k_1) + v^-(k_1, k)] X(k_1), \quad (18)$$

and $v^+(k_1, k_2)$ and $v^-(k_1, k_2)$ are the frequencies of creation and annihilation, respectively, at a column between a kink of height k_1 on the left and k_2 on the right. The stationary normal velocity of the step is given by

$$V = a \cos \theta \sum_{k_1, k_2=-\infty}^{\infty} [v^+(k_1, k_2) - v^-(k_1, k_2)] X(k_1) X(k_2), \quad (19)$$

where a is the lattice constant.

If v^+ and v^- depend only on the signs of k_1 and k_2 (negative, zero or positive), but do not depend on the height of a kink, the exact solution of Eq. (16) is again in the form (8). Moreover, taking advantage of Eqs. (2), (3) and (8) one can express $\delta = g_+ + g_-$ as a function of $\kappa = g_+ g_-$ and of the average step orientation h [5]

$$\delta = \left[\sqrt{h^2(1-\kappa)^2 + 4\kappa} - h^2(1+\kappa) \right] / (1-h^2). \quad (20)$$

The value of κ appear to depend on the choice of the v^+ and v^- frequencies. There are two different types of dynamics known from classic works on 2D MC simulations [19-24] which were later adapted to 1D simulations [6] and 1D analytical models [5]:

A) In the case of growth from vapour, no energy barrier exists for attaching the atom to the crystal and the frequency of creation does not depend on the local configuration of neighbouring atoms

$$v^+ = f_t e^{\beta-\gamma}, \quad v_i^- = v^+ \exp[\alpha(2-i)/2-\beta]. \quad (21)$$

B) If the free energy of activation of viscous flow in the mother phase is very important then the rates are symmetric

$$v_i^+ = f_t \exp[-\alpha(2-i)/4+\beta/2], \quad v_i^- = f_t \exp[\alpha(2-i)/4-\beta/2]. \quad (22)$$

In equations (21) and (22) f_t denotes a constant factor with a dimension of frequency, i is the number of nearest solid neighbours, and the conditions of crystal growth are given by Jackson-Temkin parameter α defined by Eq. (7) and the second parameter

$$\beta = (\mu_f - \mu_s)/k_B T, \quad (23)$$

where μ_f and μ_s are the chemical potentials of fluid and solid particles. In the case of 2D models, the number $i = 0, 1, 2, 3$, or 4 when the neighbour in the

previous completely solid layer is omitted. The second SOS assumption made in 1D models limits the possible values to:

$$i(k_1, k_2) = \begin{cases} 1 & \text{for } k_1 > 0 \text{ and } k_2 < 0, \\ 2 & \text{for } (k_1 > 0 \text{ and } k_2 \geq 0) \text{ or } (k_1 \leq 0 \text{ and } k_2 < 0), \\ 3 & \text{for } k_1 \leq 0 \text{ and } k_2 \geq 0. \end{cases} \quad (24)$$

The use of dynamics (21) in the kinetic equation (16) leads to

$$\kappa = \frac{e^\beta + e^{-\alpha/2}}{e^\beta + e^{\alpha/2}}. \quad (25)$$

Here we have corrected an editorial error in the formula (25) that was previously made in Ref. [5], while the other formulae and plots seem to be correct. The dynamics (21) together with Eqs. (2), (8) and (19) allow to determine the following normal velocity of the step [5]

$$V = f_t a \cos(\theta) e^{-\alpha} \left[e^\beta - \frac{(e^{\alpha/2} \kappa + e^{-\alpha/2})(1 - \delta + \kappa) + \delta - 4\kappa + \kappa\delta}{(1 - \kappa)^2} \right]. \quad (26)$$

The dynamics (22) substituted into the kinetic equation (16) leads to [5]

$$\kappa = e^{-\alpha/2}, \quad (27)$$

which means that the structure of the step is always the same as in equilibrium state ($\beta = 0$). The velocity (19) for the dynamics (22) takes the form [5]

$$V = 2f_t a \cos(\theta) \sinh(\beta/2) \frac{2e^{-\alpha/4} + \delta}{(1 + e^{-\alpha/4})^2}. \quad (28)$$

The edge free energy has not been considered in works [3-6] employing the 1D kinetic approach but the formula (14) resulting from the BCF theory may always be applied together with the results of kinetic analytical approach. Unfortunately, it is difficult to indicate any method suitable for MC simulation, where the lack of correlation between neighbouring kinks may not be assumed.

2.3. Kinetic one-dimensional Monte Carlo simulations

In 1D MC simulations the current state of solid-fluid interface is described by the array $h(x)$ stored in computer memory and updated after each random event. Therefore, the frequency of creation and annihilation are always unambiguously known for every possible location x , and the probabilities X together with the approximations (4) and (8) are no longer needed. In order to obtain the assumed step orientation θ , the ends of the array $h(0)$ and $h(N-1)$ are connected cyclically with an additional shift in the direction of the Y axis. The normal velocity of the step results directly from the increase ΔN in the number of atoms in the crystal at the time Δt [6, 21]

$$V(\theta) = \frac{a \Delta N \cos \theta}{N \Delta t}; \quad \Delta t = \sum_j \tau_j; \quad \tau_j = \sum_{i=1}^3 (n_{ij}^F v_i^+ - n_{ij}^S v_i^-), \quad (29)$$

where τ_j is the time passing between the j -th and the next elementary event, and n_{ij}^F and n_{ij}^S are numbers of fluid and solid blocks at the interface, respectively, surrounded by i solid lateral neighbours after the j -th event.

The algorithm of MC simulations of crystal growth described by Gilmer and Bennema in Ref. [19] is one of the simplest to implement, but also one of the least effective, especially for high values of the α parameter. In this work, we use an algorithm, which is a 1D version of the quick algorithm described in Ref. [21]. The choice of the algorithm, however, should affect only the time necessary to complete the simulation but not the results of simulations.

3. RESULTS AND DISCUSSION

This is known from 2D MC simulations that the layer-by-layer growth mechanism manifests itself on the (001) face of Kossel crystal when $\alpha > 3.2 \dots 3.5$ [25]. According to our best knowledge, the predictions resulting from 1D models described in section 2 have not been analyzed before for such small values of α . In addition, only the plots of the growth velocity ($V/\cos\theta$) in column direction Y (see Fig. 1) have been presented in previous papers on the kinetic approach (see *e.g.* [5, 6]), which makes it difficult to assess the normal velocity V . The $V(\theta)$ and $F(\theta)$ dependencies given by the formulas (13) and (15) resulting from the BCF theory have been used to plot some spirals growing around screw dislocations (see, *e.g.* Ref. [15]). However, the plots of these dependencies probably have not been presented and discussed anywhere.

3.1. BCF model

The dependencies derived in Chapter 2 on the basis of 1D description of the step, apply directly only to the orientations $0^\circ \leq \theta \leq 45^\circ$ [2, 15]. The use of these dependencies for any step may therefore require additional relationships resulting from the symmetry of assumed (001) face of Kossel crystal, such as *e.g.* $V(-\theta) = V(\theta)$ and $V(45^\circ - \theta) = V(45^\circ + \theta)$. However, as can be seen in Figs. 2, 4 and 5, the functions $V(\theta)$, $F(\theta)$, $d^2F(\theta)/d\theta^2$ appearing in Eq. (1) are not smooth in the extended range of θ and the results obtained for $\theta = 45^\circ + n 90^\circ$ should be considered as non-physical. Unfortunately, we cannot even say that the functions are nearly smooth with some good approximation for layer-by-layer growth mechanism when $\alpha \in 3.5 \dots 8$.

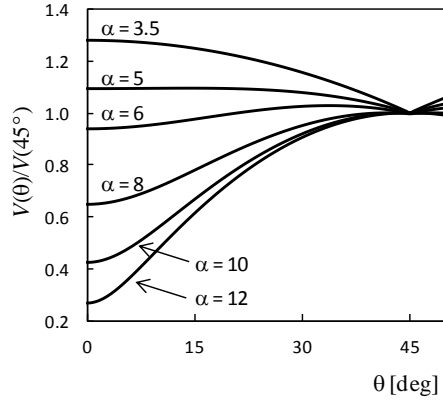


Fig. 2. Normal velocity of a step V given by Eq. (13) as a function of the step azimuth θ normalized to the level of velocity for $\theta = 45^\circ$

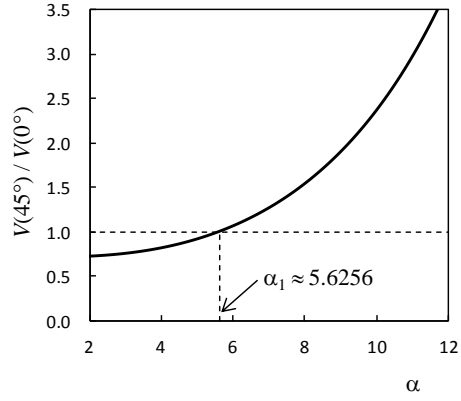


Fig. 3. Ratio of normal velocities V given by Eq. (13) for $\theta = 45^\circ$ and $\theta = 0^\circ$ as a function of the α parameter

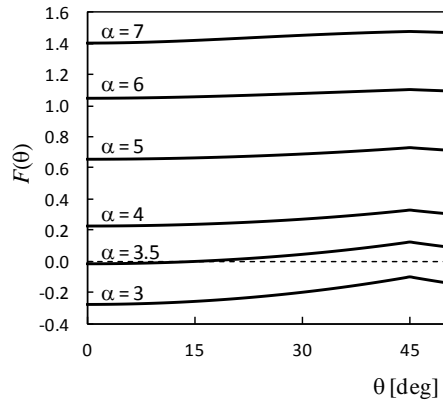


Fig. 4. Edge free energy F per unit length of a step given by Eq. (15) as a function of the azimuth θ of its orientation

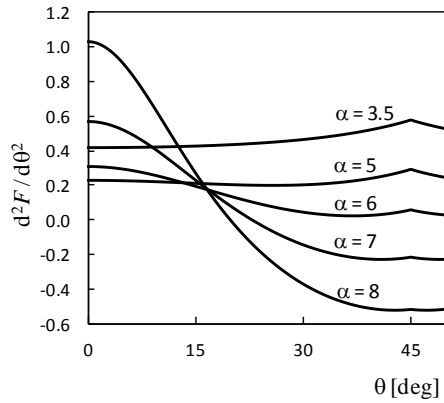


Fig. 5. The second derivative of edge free energy F per unit length of a step with respect to the azimuth θ of its orientation as a function of θ . $F(\theta)$ is given by Eq. (15)

The minimum and maximum of the $V(\theta)$ dependence can be expected for $\theta = 0^\circ$ and $\theta = 45^\circ$ [7-9, 15]. The ratio of normal velocities $V(45^\circ)/V(0^\circ)$ is therefore useful as a measure of the anisotropy of normal velocity. It can be seen in Fig. 3 that all three relations $V(45^\circ) > V(0^\circ)$, $V(45^\circ) = V(0^\circ)$ and $V(45^\circ) < V(0^\circ)$ are possible for V calculated according to Eq. (13). Because the boundary value $\alpha_1 \approx 5.6256$ for $V(45^\circ) = V(0^\circ)$ is in the area of the layer-by-layer growth mechanism, three qualitatively different cases could be expected in 2D models of spiral growth, namely: isotropic spiral and polygonized spirals with two possible orientations relative to the crystallographic axes. However, this prediction does not agree with the results of 2D MC simulations (see, e.g., Refs. [7, 9]).

3.2. Kinetic analytical approach

When the frequencies of elementary events are given by the formula (22), the kinetic approach and the BCF theory lead to the same state of the step $X(k)$ given by Eq. (8), where the g_+ and g_- factors are determined by equivalent equations (20) and (27) for the kinetic approach or (6b), (9)-(12) in the case of the BCF theory. It should be noted, however, that in the BCF theory the values of $X(k)$ were found only for equilibrium state $\beta = 0$, while in the kinetic model any value of β was allowed and the lack of dependence of $X(k)$ on β was proved.

The normal velocities $V(\theta)$ calculated according to the formula (28) from the kinetic analytical model and shown in Figs. 6 and 7 differ significantly from the velocities in Figs. 2 and 3 resulting from the formula (13). Because we compare here the velocities corresponding to the same dynamics (22) and the same state $X(k)$, the only source of observed differences lies in the two methods used to calculate the velocity. Certainly the formula (28), which takes into account various configurations of neighbouring atoms, should be considered as more accurate than the formula (13) based on total number of any kinks.

The frequencies of elementary events given by the formula (21) lead to the solution (25) and the normal velocity (26). As it can be seen in Figs. 8 and 9, the velocity is noticeably different from that in Figs. 6 and 7 corresponding to the dynamics (22). Derivation of probabilities $X(k)$ equivalent to the dynamics (21) does not seem possible on the basis of the BCF theory.

The edge free energy was not considered in previous works on the kinetic analytical approach, but we can always use the formula (14). In this way we get the same result for the dynamics (22) as in the BCF model, while the result for the dynamics (21) differs very little and the corresponding plots look like those presented in Figs. 4 and 5.

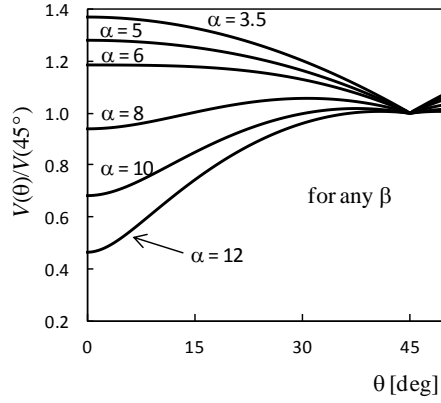


Fig. 6. Normal velocity of a step V given by Eq. (28) as a function of the step azimuth θ normalized to the level of velocity for $\theta = 45^\circ$

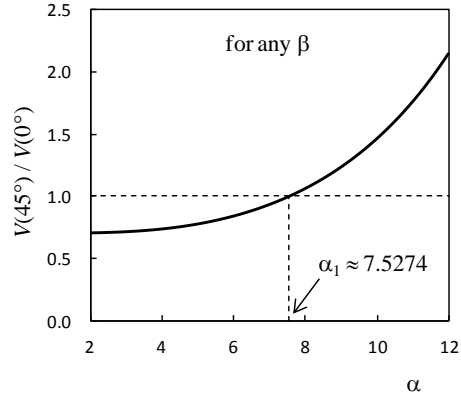


Fig. 7. Ratio of normal velocities V given by Eq. (28) for $\theta = 45^\circ$ and $\theta = 0^\circ$ as a function of the α parameter

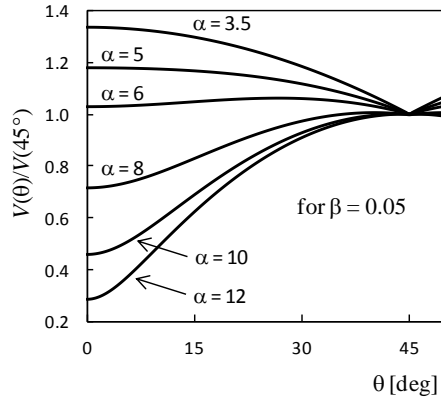


Fig. 8. Normal velocity of a step V given by Eq. (26) as a function of the step azimuth θ normalized to the level of velocity for $\theta = 45^\circ$

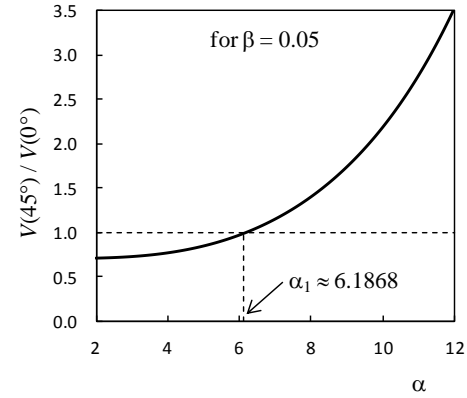


Fig. 9. Ratio of normal velocities V given by Eq. (26) for $\theta = 45^\circ$ and $\theta = 0^\circ$ as a function of the α parameter

3.3. Kinetic one-dimensional Monte Carlo simulations

The analytical model presented in section 2.2 has been evaluated in Ref. [5] as consistent for small supersaturations with the results of 1D MC simulations available in Ref. [6]. Because the data available so far were very fragmentary, in this work we present the results of our new simulations.

Comparing the plots in Figs. 10 and 11 with the plots in Figs. 6 and 7, one can notice some discrepancies between the results of 1D MC simulations and the kinetic analytical approach, which are very small for small values of α , but clearly increase with the increase of α . Our MC simulations were performed for $\beta = 0.05$, which may be considered as a small value in terms of crystal growth conditions, but it is also large enough to avoid a strong random dispersion of the results. Since the basic assumptions regarding the geometry of the system and the frequencies of elementary processes (22) are the same in both cases, the discrepancies arise from the assumption (4), which is applied only in the analytical approach.

When the dynamics (21) of elementary events is assumed, the results of 1D MC simulations shown in Figs. 12 and 13 differ only slightly from the predictions of the analytical approach presented in Figs. 8 and 9.

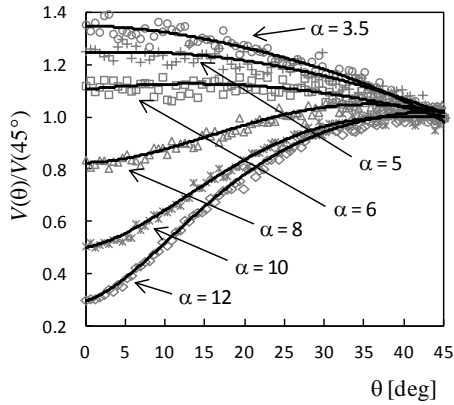


Fig. 10. Normal velocity of a step V resulting from Eq. (29) and 1D MC simulations performed for $\beta = 0.05$ and the frequencies (22) as a function of the step azimuth θ . The velocity is normalized to its level for $\theta = 45^\circ$

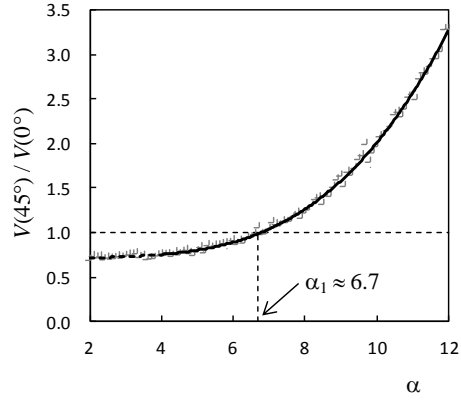


Fig. 11. Ratio of normal velocities V resulting from Eq. (29) and 1D MC simulations performed for $\beta = 0.05$ and the frequencies (22) for orientations $\theta = 45^\circ$ and $\theta = 0^\circ$ as a function of the α parameter

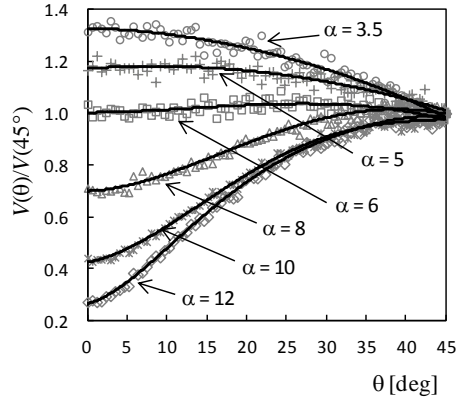


Fig. 12. Normal velocity of a step V resulting from Eq. (29) and 1D MC simulations performed for $\beta = 0.05$ and the frequencies (21) as a function of the step azimuth θ . The velocity is normalized to its level for $\theta = 45^\circ$

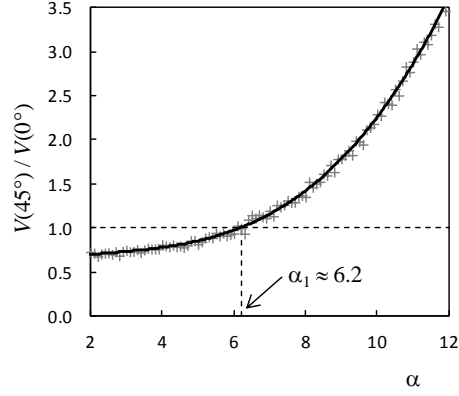


Fig. 13. Ratio of normal velocities V resulting from Eq. (29) and 1D MC simulations performed for $\beta = 0.05$ and the frequencies (21) for orientations $\theta = 45^\circ$ and $\theta = 0^\circ$ as a function of the α parameter

4. DISCUSSION

The “solid-on-solid” (SOS) assumption is commonly used in 2D models of the crystal-mother phase interface and does not lead to erroneous predictions in the area of layer-by-layer mechanism of crystal growth. The re-use of the SOS assumption for the second direction leads to a 1D description of the step on the crystal face. This simplification allowed a fully analytical derivation of the normal velocity V and of the edge free energy F of a straight step moving in any direction θ on the (001) face of Kossel crystal. The $V(\theta)$ and $F(\theta)$ dependencies are necessary, for example, to model the evolution of any step under anisotropic conditions.

However, in the light of the results presented in this paper, all approaches based on one-dimensional description, such as the BCF theory, the kinetic equation and 1D MC simulations, lead to some clearly incorrect predictions:

- 1) The normal velocity $V(\theta)$ may satisfy relations $V(0^\circ) > V(45^\circ)$, $V(0^\circ) = V(45^\circ)$ or $V(0^\circ) < V(45^\circ)$ depending on the parameters determining crystal growth conditions. The case $V(0^\circ) > V(45^\circ)$, however, is impossible to confirm based on the 2D MC simulations, which show that the spiral growing around a screw dislocation on the (001) face of the Kossel crystal can only be

isotropic or anisotropic with the orientation corresponding to the relation $V(0^\circ) < V(45^\circ)$ depending on the α and β parameters (see, e.g., Refs. [7, 9]).

- 2) The normal velocity $V(\theta)$ and the edge free energy $F(\theta)$ are not smooth functions for $\theta = 45^\circ + n 90^\circ$. The functions becomes nearly smooth only for the large values of the Jackson-Temkin parameter $\alpha > 8 \dots 10$, while the results are clearly unphysical for the remaining values of α in the area of layer-by-layer growth mechanism.

In addition, we must note some other problems appearing in the analytic models that are not directly related to the one-dimensional description of a step:

- 3) The assumption that there is no correlation between neighbouring kinks may significantly affect the obtained $V(\theta)$ dependency for high values of the α parameter.
- 4) According to the BCF theory, the entropy of a step was calculated using the Boltzmann formula $S = k_B \ln W$. However, the total energy of all bonds formed by the atoms at the edge of the step may take various levels E_i for the state described by the given set of probabilities $X(k)$. Hence, the probabilities of individual configurations should not be equal, but proportional to $\exp(-E_i/k_B T)$.

The derivation of new analytical dependencies $V(\theta)$ and $F(\theta)$, which should be free of the problems mentioned in points 1-4, is a very complicated task. Hence, it seems that future works should rather focus on determining these dependencies on the basis of 2D MC simulations and finding interpolations for a wide range of crystal growth conditions. This research direction was taken in Refs. [7-9], but the proposed form of the function $V(\theta)$ is inconsistent with the results of MC simulations for large values of θ and the relationship between the parameter of this function and crystal growth conditions is not well defined.

The movement and interaction of spirals on the crystal surface may be studied using 2D MC simulations, however, many interesting results has been also obtained by solving the equation of evolution without considering any microscopic details [10-14]. Unfortunately, recent papers are still based on the isotropic formulation of the problem known from the BCF theory of 1951. In this situation, even the use of rough approximations of the $V(\theta)$ and $F(\theta)$ dependencies could lead to progress in understanding the dynamics of spirals.

Many crystals of key importance for technology can not be described by the Kossel model of crystal. For such crystals Monte Carlo simulations are performed (see, e.g. growth of GaN modelled in Ref. [26]), while the analytical approach is not popular in the literature.

5. CONCLUSIONS

The analysis presented in this paper shows that all one-dimensional models of the step on the crystal surface lead to similar results, which are clearly non-physical for small values of the Jackson-Temkin parameter. The results, however, become more reliable with the increase in the value of this parameter. The obtained dependences can therefore be used with the step evolution equation under strongly anisotropic conditions. This approach seems promising as an extension of many previous works focused only on isotropic conditions.

REFERENCES

- [1] Frank F.C. 1949. The influence of dislocations on crystal growth. *Disc. Faraday Soc.* 5: 48-54.
- [2] Burton W.K., Cabrera N., Frank F.C. 1951. The growth of crystals and the equilibrium structure of their surfaces. *Phil. Trans. R. Soc. Lond. A* 243: 299-358.
- [3] Voronkov V.V. 1968. Non-equilibrium structure of an elementary step. *Soviet Phys. Crystallogr.* 13: 13-28.
- [4] Temkin D.E. 1969. The structure and kinetics of advance of a monomolecular step on a crystalline surface. *Soviet Phys. Crystallogr.* 14: 179-185.
- [5] Pfeifer H. 1981. Anisotropy of step motion. *Phys. stat. sol. (a)* 66: 165-173.
- [6] Esin V.O., Tarabaev L.P. 1980. Kinetics of growth of a monoatomic layer on a crystalline surface (in Russian). *Kristallografiya* 25: 357-364.
- [7] van Veenendaal E., van Hoof P.J.C.M, van Suchtelen J., van Enckevort W.J.P., Bennema P. 1998. Kinetic roughening of the Kossel (100) surface: comparison of classical criteria with Monte Carlo results. *Surface Science* 417: 121-138.
- [8] van Veenendaal E., van Hoof P.J.C.M, van Suchtelen J., van Enckevort W.J.P., Bennema P. 1999. Kinetic roughening of the Kossel (100) surface. *J. Cryst. Growth* 198/199: 22-26.
- [9] Cuppen H.M., van Veenendaal E., van Suchtelen J., van Enckevort W.J.P., Vlieg E. 2000. A Monte Carlo study of dislocation growth and etching of crystals. *J. Cryst. Growth* 219: 165-175.
- [10] Schulze T.P., Kohn. R.V. 1999. A geometric model for coarsening during spiral-mode growth of thin films. *Physica D* 132: 520-542.
- [11] Smereka P. 2000. Spiral crystal growth. *Physica D* 138: 282-301.
- [12] Forcadel N., Imbert C., Monneau R. 2012. Uniqueness and existence of spirals moving by forced mean curvature motion. *Interfaces Free Bound.* 14: 365-400.
- [13] Forcadel N., Imbert C., Monneau R. 2015. Steady state and long time convergence of spirals moving by forced mean curvature motion. *Commun. Part. Diff. Eq.* 40: 1137-1181.
- [14] Ohtsuka T., Tsai Y.-H. R., Giga Y. 2015. A level set approach reflecting sheet structure with single auxiliary function for evolving spirals on crystal surfaces. *J. Sci. Comput.* 62: 831-874.

- [15] Müller-Krumbhaar H., Burkhardt T.W., Kroll D.M. 1977. A generalized kinetic equation for crystal growth. *J. Cryst. Growth* 38: 13-22.
- [16] Jackson K.A. 1958. Mechanism of growth, in: *Liquid metals and solidification* (Ed. Moddin M.), 174-186. Cleveland: Am. Soc. for Metals.
- [17] Bennema P. 1992. Growth forms of crystals: possible implications for powder technology. *KONA Powder and Particle* 10: 25-40.
- [18] Bennema P., Gilmer G.H. 1973. Kinetics of crystal growth, in: *Crystal growth: an introduction* (Ed. Hartman P.), 263-327. Amsterdam: North-Holland Publ.
- [19] Gilmer G.H., Bennema P. 1972. Simulation of crystal growth with surface diffusion. *J. Appl. Phys.* 43: 1347-1360.
- [20] Gilmer G.H., Bennema P. 1972. Computer simulation of crystal surface structure and growth kinetics. *J. Cryst. Growth* 13/14: 148-153.
- [21] Rak M., Izdebski M., Brozi A. 2001. Kinetic Monte Carlo study of crystal growth from solution. *Comput. Phys. Commun.* 138: 250-263.
- [22] van der Eerden J.P. 1993. In: *Handbook of Crystal Growth* (Ed. Hurler D.T.J.), Vol. 1a, North-Holland, Amsterdam, p. 307.
- [23] Binsbergen F.L. 1970. A revision of some concepts in nucleation theory. *Kolloid Z. Z. Polym.* 237: 289-297.
- [24] Binsbergen F.L. 1972. Computer simulation of nucleation and crystal growth. *J. Cryst. Growth* 16: 249-258.
- [25] Bennema P. 1984. Spiral growth and surface roughening: developments since Burton, Cabrera and Frank. *J. Cryst. Growth* 69: 182-197.
- [26] Załuska-Kotur M.A., Krzyżewski F., Krukowski S. 2011. Double step structure and meandering due to the many body interaction at GaN(0001) surface in N-rich conditions. *J. Appl. Phys.* 109: 023515-1–023515-9.

WERYFIKACJA JEDNOWYMIAROWYCH MODELI OPISUJĄCYCH ANIZOTROPIĘ STOPNIA WZROSTU

Streszczenie

Dokonano przeglądu modeli znanych z literatury, które umożliwiają otrzymanie kierunkowych zależności prędkości normalnej prostoliniowego stopnia wzrostu na ścianie (001) kryształu Kossela oraz jego krawędziowej energii swobodnej. Zależności zostały rozważone w szerokim zakresie warunków wzrostu kryształu, co umożliwiło ukazanie niezgodności pomiędzy modelami oraz ograniczeń w zakresie ich stosowalności. Przedstawione wyniki koncentrują się na jednowymiarowych kinetycznych i termodynamicznych modelach pojedynczego stopnia wzrostu.

**SYLWESTER KANIA^{1,2}, BARBARA KOŚCIELNIAK-MUCHA²,
JANUSZ KULIŃSKI², PIOTR SŁOMA², KRZYSZTOF
WOJCIECHOWSKI²**

¹Institute of Physics, Lodz University of Technology, ul. Wólczńska 219,
90-924 Łódź, Poland, e-mail: skania@p.lodz.pl

²Centre of Mathematics and Physics, Lodz University of Technology,
al. Politechniki 11, 90-924 Łódź, Poland

THE EFFECT OF THE DIPOLE MOMENT ON HOLE CONDUCTIVITY OF POLYCRYSTALLINE FILMS OF TWO ANTHRACENE DERIVATIVES

Hole mobility in the polycrystalline layers of anthrone and anthraquinone differs in one order of magnitude in spite of nearly the same crystalline structure. The origin of this difference was determined with use of the quantum-mechanical calculations carried out at the density functional theory level using the B3LYP functional in conjunction with the 6-311++G(d,p) basis set. Based on these calculations, we suppose that these difference can result from the presence of the dipole moment in the anthrone molecules.

Keywords: charge carrier mobility, reorganization energy, transfer integral, anthrone, anthraquinone, TD-DFT, hole drift mobility, carrier transport, dipole moment, polycrystalline films.

1. INTRODUCTION

Anthracene derivatives can be used in organic electronics as the essential active materials for functional devices such as organic light emitting diodes (OLEDs) [1,2] or organic field-effect transistors (OFETs) [2]. Therefore, the proper understanding of the governing charge transport mechanisms in these materials is interesting from both practical and theoretical points of view. The quantity which properly explains the properties of the material in the scope of the charge transport is the electric charge mobility. Information about mobility allows to determine the macroscopic parameters of the device built with use of

the certain material. Simultaneously, the range of mobility value is dependent on the microscopic parameters such as the geometrical structure of the molecules, spatial and energetic distribution of the electrons in the molecule and the interactions between neighbouring molecules. The magnitude of the charge carrier mobility is first of all a resultant of such factors as the reorganization energy λ , charge carrier transfer integrals J_{ij} between neighbouring molecules in the lattice points i, j described as the Dexter transfer [3] and the molecules packing in the layer. However, if the molecules that built the layer have a dipole moment then the charge transfer is affected by long range interaction *i.e.* Förster transfer [4].

The Förster coupling understood as the interactions of pairs of permanent dipoles, *i.e.* between the dipole \vec{s}_1 in the centre of the coordinate system having direction s_1 in the field originated from the network of point dipoles with directions s_n may be described in the form of the sum of interactions with all other dipoles [5]:

$$\delta J_{1\alpha} = \frac{d^2}{2} \sum_{n=2}^{\infty} \left[\frac{\vec{s}_1 \vec{s}_n}{|\vec{r}_{1n}|^3} - \frac{3(\vec{s}_1 \vec{r}_{1n})(\vec{s}_n \vec{r}_{1n})}{|\vec{r}_{1n}|^5} \right], \quad (1)$$

where r_{1n} is a position of n -th dipole and α denotes a manifold of the network of point dipoles. This type of interaction may increase the dispersion of distribution of localized energy levels, what should influence a change in mobility value.

Problems presented in this paper are related to the different values of mobility in two anthracene derivatives almost identical in the crystallographic sense. The presented discussion concerns the results of quantum-mechanical calculations carried out for molecules of two compounds with significant difference in value of permanent dipole moment. Microscopic picture of phenomena occurring during transfer of charge carriers is described in the scope of Marcus-Hush theory. We treat the presence of long range Förster coupling as a modification of the model mentioned above.

Two similarly substituted aromatic hydrocarbons derived from anthracene, *i.e.* anthrone and anthraquinone were chosen as the basis of our studies. Both compounds crystallize in the nearly identical crystal lattices [6], *i.e.* monoclinic with space group $C_{2h}^5(P2_1/a)$ with bimolecular unit cell of the dimensions $a_0 = 15,8 \text{ \AA}$, $b_0 = 3,94 - 3,99 \text{ \AA}$, $c_0 = 7,865(10) \text{ \AA}$, $\beta = 102^\circ 43(2)'$ for anthraquinone and $a_0 = (15.80 \pm 0.03) \text{ \AA}$, $b_0 = (3.998 \pm 0.005) \text{ \AA}$, $c_0 = (7.86 \pm 0.16) \text{ \AA}$, $\beta = 101^\circ 40'$ for anthrone (at room temperature) [7]. The main essential difference due to the considerations discussed here is that the anthraquinone molecules, being centrosymmetric, possess dipole moment equal nearly zero,

opposite to the non-centrosymmetric anthrone molecules which are characterised by large dipole moment of 3.5 D ($1.19 \cdot 10^{-29}$ Cm) (measured in benzene) [8].

2. THEORETICAL DESCRIPTIONS

2.1. Application of the Marcus-Hush theory

Intermolecular hole transfer rate, K_{el} , during charge transport can be described on the basis of Marcus-Hush theory [9, 10] by:

$$K_{el} = \frac{4\pi^2}{h} \frac{1}{\sqrt{4\pi\lambda_+ kT}} J_{ij}^2 \exp\left(-\frac{\lambda_+}{4kT}\right), \quad (2)$$

where h is the Planck constant, k - Boltzmann constant, T - absolute temperature in Kelvin scale, J_{ij} - charge transfer integral for the hole transfer between the molecules i and j , and λ_+ refers to the reorganization energy for holes. Higher values of the hole mobility are possible when the reorganization energy λ_+ is small and the transfer integrals J_{ij} for holes are high. The reorganization energy for the hole conductivity λ_+ is calculated as the sum of two terms: λ_c for the energy needed for reorganization of the neutral molecule geometry to the cation geometry upon removal an electron and λ_n for the energy needed for reorganization to obtain cation geometry back to a neutral state upon re-accepting an electron. Therefore, in order to be able to determine the energy of reorganization for hole conductivity, it is necessary to calculate the total energy values of the molecule in the following states: optimized neutral state, E_{nn} , optimized cation state, E_{kk} , cation in the neutral geometry, E_{kn} , and the neutral molecule in the cation geometry, E_{nk} :

$$\lambda_+ = \lambda_c + \lambda_n = (E_{kn} - E_{kk}) + (E_{nk} + E_{nn}). \quad (3)$$

The transfer integral for hole conductivity, J_{ij} , can be calculated using Koopmann theorem working well independently of the distance between neighbouring molecules [11]. Its value is calculated to be equal to half of the difference between the energies of the HOMO (high occupied molecular orbital) and the next -highest occupied molecular orbital, the $\text{HOMO}^{(-1)}$ [12,13] which can be written by the following formula:

$$J_{ij} = 0.5 \cdot (\text{HOMO} - \text{HOMO}^{(-1)}). \quad (4)$$

This approach is based on tight binding formalism, assuming that the HOMO states at the ground state of neutral molecule is similar to the HOMO of the cationic species. We analyse two materials with molecules differ only by substitution group, and the presence of dipole moment, therefore the approach

presented in this article (eqs. (2), (3) and (4)) should allow us to relate transport properties to chemical structure at least qualitatively.

2.2. Computational methodology

The gas phase anthrone and anthraquinone molecules are optimized separately in the neutral and cation states using density functional theory (DFT). The calculations are conducted by means of B3LYP functional, in which Becke's three-parameter hybrid exchange functional [14] is combined with the Lee-Yang-Parr correlation functional [15]. We use a basis set with diffuse functions, namely the basis 6-311++G(d,p) as was implemented in the Gaussian 09 quantum-mechanical package [16]. Basis set with diffuse functions is important for molecular system where electrons are relatively far from nucleus, *i.e.* systems in their excited states, systems with low ionization potential. The calculations on the cationic species were performed with use of the unrestricted B3LYP formalism. The basis set with diffuse functions 6-311++G(d,p) allows theoretical determination of all parameters appearing in the Marcus-Hush equation (2), including the four energies of molecules that appear in the equation (3) and the transfer integral defined by the equation (4).

3. RESULTS AND DISCUSSION

The calculated differences of the bond lengths for anthrone and anthraquinone molecules in the gas phase in comparison to the solid state are published in [17]. We are currently presenting the visualization of the electronic clouds of the frontier orbitals of both molecules under study and of anthracene molecule properties taken as a reference. Figures 1-3 represent the occupied HOMO and HOMO⁽⁻¹⁾ orbitals and unoccupied LUMO orbitals. The visualization of frontier orbitals presented in Figs. 1-3 indicates that the electron clouds of these orbitals are concentrated on the anthracene skeleton. The anthracene molecules retain the shape of frontier orbitals in all of the considered states *i.e.* optimized neutral molecule, optimized cation, neutral molecule in cation geometry and cation in neutral molecule geometry (Fig. 3).

The shape of frontier orbitals of two derivatives of anthracene under study do not show such behaviour (Figs. 1 and 2). We note that the shape of corresponding frontier orbitals for considered two anthracene derivatives are different from that which has the unsubstituted anthracene. Such a situation is observed either for neutral molecules as for cations.

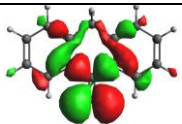
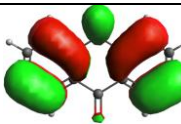
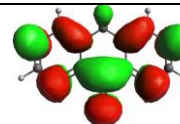
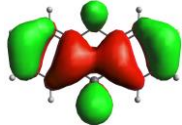
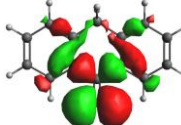
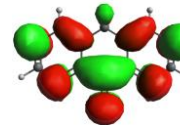
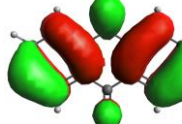
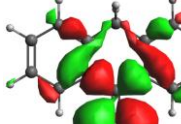
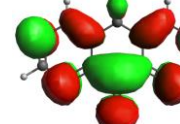
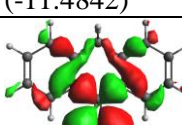
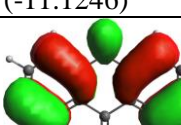
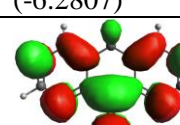
HOMO ⁽⁻¹⁾	HOMO	LUMO	
			<i>nn</i>
(-7.0425)	(-6.9928)	(-2.1437)	
			<i>kn</i>
(-11.5403)	(-11.0816)	(-6.3318)	
			<i>kk</i>
(-11.4842)	(-11.1246)	(-6.2807)	
			<i>nk</i>
(-7.0818)	(-6.8230)	(-2.1004)	

Fig. 1. Frontier orbitals having direct participation in electron transitions in anthrone, calculated orbitals energies are given in eV (*nn* - optimized geometry of neutral molecule, *kk* - optimized cation, *kn* - cation in the geometry of neutral state, *nk* - neutral molecule in geometry of cation)

The asymmetry of substitution in the anthrone molecule is clearly manifested in the asymmetry of the spatial distribution of its frontier orbitals. The presence of this asymmetry is seen in the greater increase in the number of nodal points in the space distribution of frontier orbitals for anthraquinone in neutral forms than for the cation forms. The removal of the electron from a molecule has a considerable effect on the energy of all orbitals, strongly reducing this energy. All cation orbitals are binding, what means the stability of both the molecule in a neutral state and being a cation. However, the energy differences between them are maintained, *i.e.* between the energy levels of HOMO and HOMO⁽⁻¹⁾ and between the energy levels of LUMO and HOMO for all calculated structures of a given molecule.

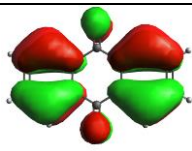
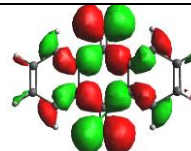
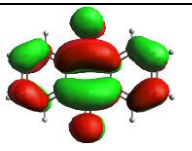
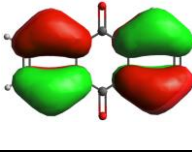
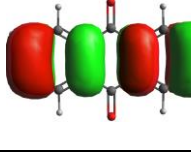
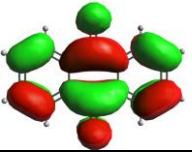
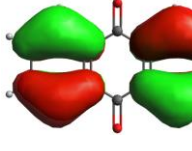
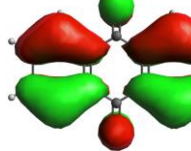
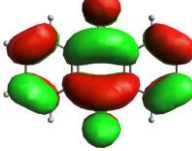
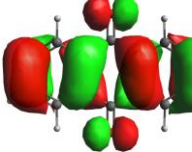
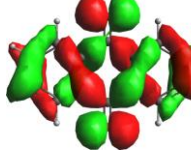
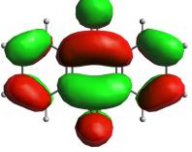
HOMO ⁽⁻¹⁾	HOMO	LUMO	
			<i>nn</i>
(-7.5786)	(-7.3969)	(-3.1865)	
			<i>kn</i>
(-11.8502)	(-11.7825)	(-7.9882)	
			<i>kk</i>
(-11.9545)	(-11.7989)	(-7.7414)	
			<i>nk</i>
(-7.5898)	(-7.3144)	(-3.1421)	

Fig. 2. Frontier orbitals having direct participation in electron transitions in anthraquinone. Calculated orbitals energies are given in eV (*nn* - optimized geometry of neutral molecule, *kk* - optimized cation, *kn* - cation in the geometry of neutral state, *nk* - neutral molecule in geometry of cation)

Reorganization energies for hole conductivity calculated for the molecules of anthrone, anthraquinone and anthracene are presented in Table 1, whereas in Table 2 the values of the hole transfer rate for above mentioned compounds, calculated with use of the procedure exploits the formulas (1) and (2), are presented.

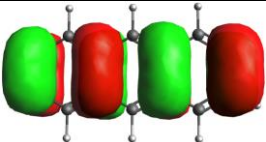
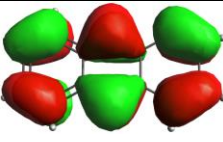
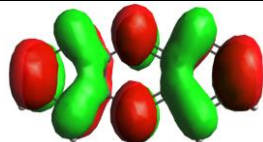
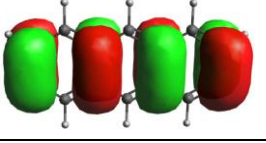
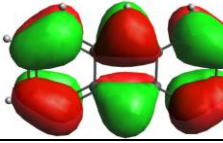
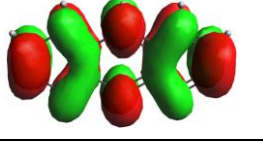
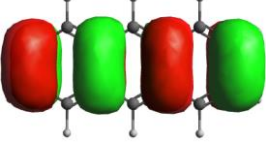
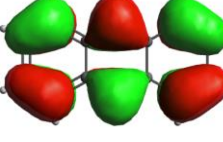
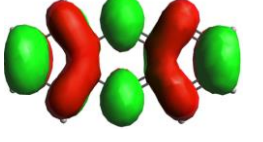
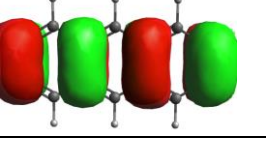
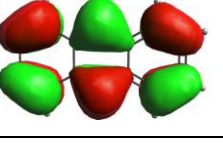
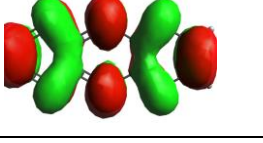
HOMO ⁽⁻¹⁾	HOMO	LUMO	
			<i>nn</i>
(-6.7503)	(-5.5538)	(-1.9355)	
			<i>kn</i>
(-11.1330)	(-10.2922)	(-6.6254)	
			<i>kk</i>
(-11.836)	(-10.1681)	(-6.777)	
			<i>nk</i>
(6.8678)	(-5.4415)	(-2.1568)	

Fig. 3. Frontier orbitals having direct participation in electron transitions in anthracene, calculated orbitals energies are given in eV (*nn* - optimized geometry of neutral molecule, *kk* - optimized cation, *kn* - cation in the geometry of neutral state, *nk* - neutral molecule in geometry of cation)

On the basis of the results presented in the tables we can conclude that the reorganization energy for anthrone is higher by 0.040 eV than that for anthraquinone. The transfer rate for holes is higher by one order of magnitude for anthraquinone $K_{el} = 1.020 \cdot 10^{14}$ Hz, than for anthrone, $K_{el} = 4.659 \cdot 10^{12}$ Hz. The above would suggest that the hole transfer under unit electric field in anthraquinone should be easier. Experimental results presented in Table 3 suggest that the hole mobility in anthrone is much greater than in anthraquinone. The hole mobility for anthrone $\mu = (7 \pm 2) \cdot 10^{-3} \text{ cm}^2(\text{Vs})^{-1}$ is almost one order of magnitude higher than for anthraquinone, $\mu = (8 \pm 2) \cdot 10^{-4} \text{ cm}^2(\text{Vs})^{-1}$. The

anthrone molecule in comparison to the molecule of anthraquinone possess strong dipole moment, whose value measured in benzene is $\mu_d = 3.5$ D in comparison to the almost zero value of the dipole moment for anthraquinone. Taking into account the above consideration, it can be assumed that the correction of the Förster transfer in the formula for the transfer integral for charge carrier transfer can't be neglected and it can be assumed that magnitude of the mobility value is strongly influenced by the dipole moment.

Table 1

The results of quantum-mechanical calculations (functional B3LYP/6-311++(G(d,p)): orbitals energy levels of HOMO and LUMO as well as the reorganization energy for hole conductivity, vertical ionization energy IP_v and vertical electron affinity EA_v .

compound	HOMO	LUMO	Reorganization energy for hole conductivity, λ_+	IP_v	EA_v
	[eV]	[eV]	[eV]	[eV]	[eV]
anthrone	-6.992	-2.144	0.173	-8.59	-0.57
anthraquinone	-7.396	-3.186	0.135	-9.09	-1.60
anthracene	-5.553	-1.936	0.139 (0.136 [11])	-7.16	-0.49

Table 2

Calculation of the hole transfer rate with use the formulas (1) and (2)

compound	J_{ij} [eV]	J_{ij}^2 [eV ²]	λ [eV]	$\exp(-\lambda/(4kT))$	K_{el} [Hz]
anthrone	0.0249	$6.199 \cdot 10^{-4}$	0.173	0.1873	$4.659 \cdot 10^{12}$
anthraquinone	0.0909	$8.260 \cdot 10^{-3}$	0.135	0.2715	$1.020 \cdot 10^{14}$
anthracene	0.5982	$3.579 \cdot 10^{-1}$	0.139	0.2611	$4.187 \cdot 10^{15}$

Table 3

Experimentally obtained hole mobility values in the polycrystalline layers of anthrone and anthraquinone [18])

compound	μ [cm ² (Vs) ⁻¹]
anthrone	$(7 \pm 2) \cdot 10^{-3}$
anthraquinone	$(8 \pm 2) \cdot 10^{-4}$

ACKNOWLEDGEMENTS

We would like to express gratitude to prof. B. Marciniak and dr Ewa Różycka-Sokołowska for valuable discussions and to prof. Wieczorek for preparation of the spectral grade anthraquinone and anthrone and for enabling the X-ray analysis.

The calculations presented in this paper are performed using the PLATON project's infrastructure at the Computer Center of Lodz University of Technology.

REFERENCES

- [1] Dadvand A., Moisev A.G., Sawabe K., Sun W-H., Djukic B., Chung I., Takenobu T., Rosei F., Perepichka D.F. 2012. Maximizing Field-Effect Mobility and Solid-State Luminescence in Organic Semiconductors. *Angew. Chem. Int. Ed.* 51: 3837-3841.
- [2] Aleshin A.N., Lee J.Y., Chu S.W., Kim J.S., Park Y.W. 2004. Mobility studies of field effect transistor structures based on single crystals, *Appl. Phys. Lett.* 84: 5383-5385.
- [3] Dexter DL. 1953. A Theory of Sensitized Luminescence in Solids. *J. Chem. Phys.* 21:836-850.
- [4] Förster T. 1948. Zwischenmolekulare Energiewanderung und Fluoreszenz. *Ann Phys.* 437:55-75.
- [5] Stehr V., Fink R.F., Tafipolski M., Deibel C., Engels B. 2016. Comparison of different rate constant expressions for the prediction of charge and energy transport in oligoacenes. *WIREs. Comput. Mol. Sci.* 6: 694-720.
- [6] Flack H.D. 1970. I. Refinement and thermal expansion coefficients of the structure of anthrone (20, -90°C) and comparison with anthraquinone, *Phil. Trans. A* 266: 561-574.
- [7] Srivastava S.N. 1964. Three-dimensional refinement of the structure of anthrone. *Acta Cryst.* 17: 851-856.
- [8] Angyal C.L., Le Fevre R.J.W. 1950. The polarities of enols. *J. Chem. Soc.* 106: 562-564.
- [9] Marcus R.A. 1997. Electron transfer reactions in chemistry. Theory and experiment. *Pure & Appl. Chem.* 69: 13-29.
- [10] Hush N.S. 1958. Adiabatic Rate Processes at Electrodes. I. Energy-Charge Relationships, *J. Chem. Phys.* 28: 962-972.
- [11] Raughnath P., Reddy M.A., Gouri C., Bhanuprakash K., Rao V.J. 2006. Electronic properties of anthracene derivatives for blue light emitting electroluminescent layers in organic light emitting diodes: a density functional study. *J. Phys. Chem.* 110: 1152-1162.
- [12] Deng W-Q., Goddard III A. 2004. Predictions of Hole Mobilities in Oligoacene Organic Semiconductors from Quantum Mechanical Calculations. *J. Phys. Chem. B* 108: 8614-8621.

- [13] Kirkpatrick J., Nelson J. 2005. Theoretical study of the transfer integral and density of states in spiro-linked triphenylamine derivatives. *Journal of Chemical Physics* 123: 084703.
- [14] Becke A.D. 1993. Density-functional thermochemistry. III. The role of exact exchange. *J. Chem. Phys.* 98: 5648.
- [15] Lee C., Yang W. Parr R. 1988. Development of the Colle-Salvetti correlation-energy formula into a functional of the electron density. *Phys Rev. B* 37: 785-789.
- [16] Frisch M.J. et. al. 2009. Gaussian 09, Revision A.02, Gaussian Inc. Wallingford CT.
- [17] Kania S., Kościelniak-Mucha B., Kuliński J., Słoma P., Wojciechowski K. 2016. The effect of symmetry of a molecule electronic density on the dipole moment of unit cell, and hole conductivity of thin polycrystalline films of anthrone and anthraquinone. *Sci. Bull. Lodz Univ. Tech. Physics* 37: 49-64.
- [18] Kania S. 2014, Hole drift mobility in anthrone and anthrachinone layers with different structure. *Sci. Bull. Lodz Univ. Tech. Physics* 35: 17-24.

WPŁYW MOMENTU DIPOŁOWEGO NA PRZEWODNICTWO DZIUR W WARSTWACH POLIKRYSTALICZNYCH DWU POCHODNYCH ANTRACENU

Streszczenie

Ruchliwość dziur w polikrystalicznych warstwach antronu i antrachinonu różni się prawie o jeden rząd wielkości, pomimo niemal tej samej struktury krystalicznej. Źródło tej różnicy próbowano określić przy użyciu obliczeń kwantowo-mechanicznych przeprowadzonych na poziomie teorii funkcjonału gęstości (DFT) z wykorzystaniem funkcjonału B3LYP, stosując funkcje bazy 6-311++G(d,p). Na podstawie tych obliczeń przypuszczamy, że ta różnica jest wynikiem obecności momentu dipolowego w cząsteczkach antronu.

**SYLWESTER KANIA^{1,2}, JANUSZ KULIŃSKI^{2,3},
DOMINIK SIKORSKI⁴**

¹Institute of Physics, Lodz University of Technology, ul. Wólczńska 219, 90-924, Łódź, Poland, e-mail: sylwester.kania@p.lodz.pl

²Centre of Mathematics and Physics, Lodz University of Technology, al. Politechniki 11, 90-924 Łódź, Poland, e-mail: janusz.kulinski@p.lodz.pl

³The Faculty of Mathematics and Natural Sciences, Jan Długosz University in Częstochowa, al. Armii Krajowej 13/15, 42-218 Częstochowa, Poland

⁴Faculty of Electrical, Electronic, Computer and Control Engineering Lodz University of Technology, ul. Bohdana Stefanowskiego 18/22, 90-924 Łódź, Poland

COMPARATIVE STUDY OF THE INFLUENCE OF THE REORGANIZATION ENERGY ON THE HOLE TRANSPORT OF TWO FOUR-CYCLIC ARENES

Application of the method of quantum-mechanical calculations allowed the determination of the reorganization energy of the molecules of tetracene and p-quaterphenyl and the estimation of the transfer rate integral between neighbouring molecules present in the solid state. Comparison of the transfer rates for holes with the values of the mobility, obtained experimentally for the polycrystalline tetracene layers and p-quaterphenyl layers vaporized in the vacuum in the similar conditions indicate that the molecule's structure possess the dominate impact on the conductivity of the thin layers of these compounds.

Keywords: reorganization energy, tetracene, p-quaterphenyl, carrier mobility.

1. INTRODUCTION

Arenes have been studied for many years for potential applications in organic electronics. This perspective stimulates research on their electronic and photophysical properties [1-3]. Theoretical calculations using computational methods of quantum-mechanics can contribute to our understanding of the electronic processes decisive on charge carriers transport [4-5]. Electronic

structure of arene molecules have been studied in numerous papers. In this work we focus on finding the origin of the observed difference in the hole mobility values in the thin layers of intrinsic four cyclic arenes. This study is focused on two non-substituted arenes built from four linearly arranged benzene rings, i.e. p-quaterphenyl and tetracene.

Tetracene moiety is built of the rigid skeleton, but p-quaterphenyl moiety is built of the rings which all can rotate. The choice of these compounds is related to the fact that both studied compounds crystallize in a similar crystal lattice with identical motif of “herring bone” arrangement.

Tetracene, with chemical formula $C_{18}H_{12}$ and molecular weight 228.29 g/mol, belongs to triclinic crystal system $P\bar{1}$, $a = 6.0565 \pm 0.0009$ Å, $b = 7.8376 \pm 0.0011$ Å, $c = 13.0104 \pm 0.0018$ Å, $\alpha = 77.127 \pm 0.002^\circ$, $\beta = 72.118 \pm 0.002^\circ$, $\gamma = 85.792 \pm 0.002^\circ$ [6]. The durability of the solid phase is evidenced by its thermodynamic parameters [7] such as melting point 623 K, enthalpy of fusion $\Delta_{fus}H_m(T_{fus}) = 35.9$ kJ/mol and enthalpy of vaporization $\Delta_{vap}H_m(298\text{ K}) = 87.4$ kJ/mol. Such durability of the layers in the conditions of electronic devices using layered structures [8] allows to treat this material as very promising for future-oriented applications in organic electronics.

P-quaterphenyl with chemical formula $C_{24}H_{18}$ and molecular weight 306.40 g/mol, belongs to monoclinic structure $P2_1/a$, $a = 8.110 \pm 0.006$ Å, $b = 5.610 \pm 0.004$ Å, $c = 17.910 \pm 0.010$ Å, $\beta = 95.80 \pm 0.06^\circ$ [9,10]. Its thermodynamic parameters including melting point 593 - 594 K and enthalpy of fusion $\Delta_{fus}H_m(T_{fus}) = 57.6 \pm 0.9$ kJ/mol and the enthalpy of vaporization $\Delta_{vap}H_m(298\text{ K}) = 136.1 \pm 3.2$ kJ/mol [7], indicate its stability at room temperatures at which the layers are prepared. They do not show desorption properties up to 360 K during deposition on the Au electrode [11]. Both selected compounds have very similar crystalline characteristics such as packing density and coordination number. They differ only in the rigidity of the molecule skeleton.

2. COMPUTATIONAL PROCEDURES

2.1. Theoretical model

The real mechanism for charge transfer in solid organic materials is often difficult to determine. Generally speaking, in the high temperature limit it is assumed that in π -conjugated organic semiconductors where intermolecular interactions are formed as a result of the presence of weak bonds, the hopping transport is dominated [12]. Such a mechanism of transport is postulated in the

Marcus-Hush model. In compliance with this model the process of transfer of charge carriers through the molecule is connected with two consecutive processes. The first one, related to the internal reorganization energy λ , is relaxation to the state of dynamic equilibrium of the electronic cloud in the molecule, the second one, described by the external energy of reorganization λ_z , is readjustment of the spatial distribution of the nuclei of the atoms that built the molecule to the changed distribution of electron clouds in the molecule. However, the process of charge transfer between neighbouring molecules, related to the overlap of frontier orbitals of these molecules, is described by the transfer integral J_{ij} [2]. The weak bonds existing between molecules are weaker than the covalent bonds inside the molecule. Therefore, the calculation of the energy levels of gas molecules can be used to determine the solid phase transport of the charge carriers in the solid phase [13-14]. Such an approximation allows to conduct the quantum-mechanical calculations and leads to calculations of the values of reorganization energy for hole conductivity in the solid phase using calculations made only for a single molecule in the gas phase. Reorganization energy is a useful tool for description of the transport of both electrons and holes for majority of organic materials, where the hopping transport model can be applied. This is connected with strong localization of the charge in all of the molecules taking part in the conductivity process. Process of transferring charge in the gradient of electric field may be described from the chemical point of view as a series of successive reactions red-ox with transfer of charge [3].

Reorganization energy for hole transport λ_+ may be treated as the sum of two terms, λ_{1+} and λ_{2+} :

$$\lambda_+ = \lambda_{1+} + \lambda_{2+} = (E_0^+ - E_+^+) + (E_+^0 - E_0^0). \quad (1)$$

In the above equation, E_0^0 i E_+^+ mean the total energy of the neutral molecule and the cation in their equilibrium structures, respectively, while E_0^+ means the total energy of cation in the neutral molecule geometry, and E_+^0 means the total energy of neutral molecule in the cation geometry. The first term, λ_{1+} , corresponds to the process of cation radical formation, and the second term, λ_{2+} , corresponds to the relaxation of the charged state. The hole transfer rate, K_{el} , seen during the charge carrier transport process may be defined in the scope of the Marcus theory with use of the formula [4]:

$$K_{el} = \frac{4\pi^2}{h} \frac{1}{\sqrt{4\pi\lambda_+kT}} J_{ij}^2 \exp\left(-\frac{\lambda_+}{4kT}\right), \quad (2)$$

where h is Planck constant, k - Boltzmann constant, T - temperature in kelvins, J_{ij} - electron transfer integral calculated between i and j nodes, and λ_+ is reorganization energy for hole and electron. For occurrence of good hole conductivity reorganization energy λ_+ should be low, but the value of the charge transfer energy J_{ij} should be high.

2.2. Quantum-mechanical calculations

In order to determine the internal and external energy values of the reorganization energy for p-quaterphenyl and tetracene calculation of the total energy of the molecule being in neutral or ionized state in the gas phase with use of Eq. (1) is necessary. These calculations were carried out with use of Gaussian-09 package. Since both molecules considered here contains less than 50 atoms, therefore a convenient calculation method is density functional theory (DFT) with use of the B3LYP functional. The B3LYP functional is considered to be excellent in such application and has been applied in many works to calculate the basic states of aromatic hydrocarbons molecules. It is also used in calculations of excited states [15]. Due to the complex range of calculations the functional B3LYP/6-311++G(d,p) was used, with diffusion functions for heavy atoms as well as hydrogen atoms. This approach allowed us to calculate both the distribution of electrons at given position of the nuclei of the atoms forming the molecule and the optimization of the molecule in neutral and ionized state. This level of theory gives a good agreement between the experiment and the calculated energies of orbitals for polycyclic hydrocarbons [4, 5].

3. RESULTS AND DISCUSSION

It has been obtained as a result of optimization using quantum mechanical calculations, that in the case of anthracene and p-quaterphenyl the minimum energy is achieved for plane structures. The benzene rings that form the skeleton of p-quaterphenyl molecule did not show rotation. Both tested molecules did not show a dipole moment.

3.1. Electronic properties

Both the p-quaterphenyl and the tetracene molecules are highly stable. The HOMO energy levels in p-quaterphenyl as well as in tetracene are below -5.1 eV. This low level of HOMO energy indicates the resistance of the studied molecules in respect to atmospheric factors. Resistance of this kind is revealed

during conduction of holes, i.e. using both of molecules as forming layers of a p-type semiconductor [16]. Unfortunately, the high LUMO level energy value above -3 eV, for both tested compounds shows low resistance to atmospheric factors during electron conduction. The lower LUMO level for tetracene ($E_{\text{LUMO}} = -2.401$ eV), indicates its better resistance to atmospheric factors during electron conduction than in the case of p-quaterphenyl ($E_{\text{LUMO}} = -1.951$ eV).

Table 1

Parameters of electron levels in molecules. Frontier orbitals energies: $\text{HOMO}^{(0)}$, $\text{HOMO}^{(-1)}$, $\text{LUMO}^{(0)}$, $\text{LUMO}^{(-1)}$ and the energy of forbidden states for neutral molecule, $\Delta E^{(0)} = \text{LUMO}^{(0)} - \text{HOMO}^{(0)}$, $\Delta E^{(-1)} = \text{LUMO}^{(-1)} - \text{HOMO}^{(-1)}$

	p-quaterphenyl	tetracene
$\text{HOMO}^{(0)}$ (eV)	-5,754	-5,141
$\text{LUMO}^{(0)}$ (eV)	-1,951	-2,401
$\Delta E^{(0)}$ (eV)	3,804	2,740
$\text{HOMO}^{(-1)}$ (eV)	-6,659	-6,759
$\text{LUMO}^{(-1)}$ (eV)	-1,011	-0,812
$\Delta E^{(-1)}$ (eV)	5,548	5,947

Table 2 presents calculated parameters describing the possibility of disconnecting the electron from the molecule, IP (ionization potential of the molecule), electron connection to the molecule, EA (electron affinity energy) and two components of reorganization energy: λ_{+1} , λ_{+2} calculated according to formula (1).

Table 2

The parameters describing the effect of molecular structure on hole transport

	p-quaterphenyl	tetracene
IP (eV)	13.865	13.064
EA (eV)	0.957	2.113
λ_{+1} (eV)	0.108	0.054
λ_{+2} (eV)	0.105	0.053

The values collected in Table 3 allow to calculate the charge transfer rate according to formula (3) [17]

$$J_{ij} = 0,5 (\text{HOMO}^{(0)} - \text{HOMO}^{(-1)}) \quad (3)$$

Analysis of the obtained values indicates that the value of hole transfer rate, calculated with accordance of the formula (2), is significantly different for both

studied molecules. For tetracene, this value is $1.19 \cdot 10^{16}$ Hz and it is of order of magnitude greater than for p-quaterphenyl, for which it is equal $9.58 \cdot 10^{14}$ Hz. A similar difference, also of an order of magnitude, is observed for experimentally determined mobility values, for layers of these materials obtained under similar conditions and having a polycrystalline structure. For tetracene, the experimentally determined drift mobility is $\mu = 1.6 \cdot 10^{-3} \text{ cm}^2 \text{Vs}^{-1}$ [18], while for p-quaterphenyl this value is one order of magnitude lower and is equal to $\mu = 9 \cdot 10^{-5} \text{ cm}^2 \text{Vs}^{-1}$ [19].

Table 3
Comparison of the impact of the reorganization energy value and the value of the overlap integral on the hole transfer rate value K_{el} . For comparison, the table presents experimental values of mobility

	p-quaterphenyl	tetracene
$J_{ij} = 0.5(\text{HOMO}^{(0)} - \text{HOMO}^{(-1)}) [\text{eV}]$	0.453	0.809
$J_{ij}^2 [\text{eV}^2]$	0.205	0.654
$\lambda = \lambda_{+1} + \lambda_{+2} [\text{eV}]$	0.212	0.107
$K_{el} [\text{Hz}]$	$9.58 \cdot 10^{14}$	$1.19 \cdot 10^{16}$
$\mu [\text{cm}^2 \text{Vs}^{-1}]$	$9.0 \cdot 10^{-5}$	$1.6 \cdot 10^{-3}$

4. CONCLUSIONS

The values obtained by calculations of reorganization energy values λ_+ for holes and values of the transfer integral J_{ij} indicate much easier conduction of holes in tetracene with respect to conduction of holes in p-quaterphenyl. The similar ratio of the speed of transferring holes $K_{el}(\text{tetracene})/K_{el}(\text{p-quaterphenyl}) = 1.19 \cdot 10^{16}/9.58 \cdot 10^{14} = 12.4$, as well as mobility ratio $\mu(\text{tetracene})/\mu(\text{p-quaterphenyl}) = 1.6 \cdot 10^{-3}/9 \cdot 10^{-5} = 17.8$ indicate a similar effect of disordered particles on the transport of holes in the polycrystalline layers of both materials.

ACKNOWLEDGEMENTS

The results of our own calculations included in this study were obtained thanks to the PLATON project infrastructure in the Computer Center of the Lodz University of Technology.

REFERENCES

- [1] O'Neill L., Lynch P., McNamara M., Byrne H.J. 2005. Structure Property Relationships in Conjugated Organic Systems, *Synth. Metals* 153: 289-292.
- [2] Watson M.D., Fechtenkötter A., Müllen K. 2001. Big Is Beautiful - "Aromaticity" Revisited from the Viewpoint of Macromolecular and Supramolecular Benzene Chemistry. *Chem. Rev.* 101: 1267-1300.
- [3] Roncali J., Leriche P., Blanchard P. 2014. Molecular Materials for Organic Photovoltaics: Small is Beautiful. *Adv. Mater.* 26: 3821-3838.
- [4] Coropceanu V., Cornil J., da Silva Filho D.A., Olivier Y., Silbey R., Bredas J-L. 2007. Charge Transport in Organic Semiconductors. *Chem. Rev.* 107: 926-952.
- [5] Zhao C., Guo Y., Guan L., Ge H., Yin S., Wang W. 2014. Theoretical investigation on charge transport parameters of two novel heterotetracenes as ambipolar organic semiconductors. *Synth. Metals* 188: 146-155.
- [6] Holms D., Kumaraswamy S., Matzger A.J., and Vollhardt K.P.C. 1999. On the nature of nonplanarity in the [N]Phenylenes. *Chem. Eur. J.* 5: 3399-3412.
- [7] Roux M.W., Temprado M., Chickos J.S., Nagano Y. 2008. *J. Phys. Chem. Ref. Data* 37: 1855-1996.
- [8] Tersigni A., Shi J., Jiang D.T., Qin X.R. 2006. Structure of tetracene films on hydrogen-passivated Si(001) studied via STM, AFM, and NEXAFS. *Phys. Rev. B* 74: 205326-1 - 205326-9.
- [9] Delugeard Y., Desuche J., Baudour J.L. 1976. Structural transition in polyphenyls. II. The crystal structure of the high-temperature phase of quaterphenyl. *Acta Cryst. B* 32: 702-705.
- [10] Kawaguchi A., Tsui M., Moriguchi S., Uemura A., Isoda I., Ohara M., Petermann J., Katayama K. 1986. Electron Microscopical Studies on p-Polyphenyls. *Bull. Inst. Chem. Res., Kyoto Univ.* 64: 54-65.
- [11] Müllergger S., Stranik O., Zojer E., Winkler A. 2004. Adsorption, initial growth and desorption kinetics of p-quaterphenyl and polycrystalline gold surfaces. *Appl. Surf. Sci.* 221: 184-196.
- [12] Köhler A., Bässler H. 2011. What controls triplet exciton transfer in organic seiconductors? *J. Mater. Chem.* 21: 4003-4011.
- [13] Skobel'tsyn Z.G. 1965. The oriented gas model and its application to molecular crystals. in: *Proceedings of the Lebedev Physics Institute*, vol. 25: Optical methods of investigating solid bodies, ed. Skobel'tsyn Z.G., Chapter III, pp.44-66. Consultants Bureau Enterprises, Inc. New York.
- [14] Ostroverkhova O. 2016. *Chem. Rev.* 116: 13279 -13412.
- [15] Mallocci G., Cappellini G., Mulas G., Mattoni A. 2011. Electronic and optical properties of families of polycyclic aromatic hydrocarbons: a systematic (time-dependent) density functional theory study. *Chem. Physics* 384: 19-27.
- [16] Takimiya K., Osaka I., Nakano M. 2014. π -Building Blocks for Organic Electronics: Revaluation of "Inductive" and "Resonance" Effects of π -Electron Deficient Units. *Chem. Mater.* 26: 587-593.

- [17] Deng W-Q., Goddard III A. 2004. Predictions of Hole Mobilities in Oligoacene Organic Semiconductors from Quantum Mechanical Calculations, *J. Phys. Chem. B* 108: 8614-8621.
- [18] Kania S. 2007, Charge carrier transport in the tetracene layers with different structural order, *Visnik Lviv Univ. Ser. Physics* 40: 322-336.
- [19] Kania S., Kondrasiuk J., Bąk G.W. 2004. Influence of ambient atmosphere on charge transport in polycrystalline thin films of three simple aromatic hydrocarbons. *Eur. Phys. J. E* 15: 439-442.

STUDIUM PORÓWNAWCZE WPŁYWU ENERGII REORGANIZACJI NA PRZEWODNICTWO DZIUR DWU CZTEROPIERŚCIENIOWYCH ARENÓW

Streszczenie

Zastosowanie metody obliczeń kwantowo-mechanicznych pozwoliło na wyznaczenie energii reorganizacji cząsteczek tetracenu i p-kwaterfenylu oraz oszacowanie wartości całki przenoszenia elektronu pomiędzy sąsiadującymi cząsteczkami znajdującymi się w fazie stałej. Porównanie szybkości przenoszenia dziur z wartościami ruchliwości dziur w polikrystalicznych warstwach tetracenu i p-kwaterfenylu naparowanych w próżni w identyczny sposób wskazuje na dominujący wpływ budowy cząsteczki na przewodnictwo cienkich warstw tych związków.

**SYLWESTER KANIA^{1,2}, BARBARA KOŚCIELNIAK-MUCHA²,
JANUSZ KULIŃSKI², PIOTR SŁOMA²,
KRZYSZTOF WOJCIECHOWSKI²**

¹Institute of Physics, Lodz University of Technology, ul. Wólczńska 219,
90-924 Łódź, Poland, e-mail: sylwester.kania@p.lodz.pl

²Centre of Mathematics and Physics, Lodz University of Technology,
al. Politechniki 11, 90-924 Łódź, Poland, e-mail: janusz.kulinski@p.lodz.pl

SENSITIVITY OF TETRACENE LAYER AS AN EFFECT OF ENTANGLEMENT

Application of the method of quantum-mechanical calculations allowed for studies of variability of interactions between molecules of ethanol and tetracene. Entanglement of quantum states is seen during calculations in two ways: as a change of electric dipole moment and as an increase of the basis set superposition error (BSSE) with decreasing distance between molecules under study. There are observed the dependences of the total energy of the system due to the mutual arrangement of the long axes of the molecules and due to the orientation of the bond of the oxygen atom to the carbon atom with respect to the plane of benzene skeleton of tetracene molecule.

Keywords: quantum-mechanical-calculations, tetracene, ethanol, basis set superposition error.

1. INTRODUCTION

The demand for reusable gas sensors stimulates the development of existing and new technologies for the production of such type of sensors. The basic types of chemical sensors include the active layer of the transducer. Multiple phenomena occur as a result of interaction with the ambient gas. Final effects of them are transformed into an electrical signal. A useful electronic signal shows frequency variation, current change or voltage change. Gas detection technologies use semiconductor type: catalytic, electrochemical and acoustic gas sensors [1]. For economic reasons, the desirable property of sensors is the possibility of their multiple use. The possibility of obtaining such sensors is available when the adsorption process taking place in the adsorbent layer is

reversible. Such properties are exhibited *e.g.* by pentacene layers for the adsorption of water molecules [2]. A similar phenomenon was observed for tetracene layers [3] where enhancement in the conductivity of thin films was caused by ethanol adsorption. Kania and Kuliński [4] proposed that the adsorption and charge transfer process was related to mutual collisions of ethanol molecules in the adsorption layer, and to the dissociation of the ethanol molecule on the surface of tetracene. They showed that the increase in the conductivity of the tetracene layer depends on the concentration of active activator molecules (ethanol). The time constant for the adsorption at the starting point was 30.8 s at the ethanol vapour pressure of 0.2 Tr at room temperature, whereas the desorption time constant was only 11.3 s when the pressure obtained a value of 10^{-5} Tr. The low value of the time constant for desorption is puzzling due to the presence of a significant activation energy for adsorption of $\Delta H = 84$ kJ/mol, demonstrating the presence of weak chemisorption. The problem needs to be explained on the basis of quantum-mechanical calculations.

The problem of the adsorption mechanism is complex and requires considering the adsorbent particles forming the solid surface and the adsorbed molecules in the form of gas molecules as a quantum system. This type of problem can be solved only by quantum-mechanical calculations. A convenient tool for solving such a problem is the density functional theory method (DFT) [5-7].

In the presented article, we have taken up the problem of the emergence and increase of interactions between the upcoming ethanol molecule and the tetracene molecule. Both of the approaching particles are not pointwise. Each molecule has an internal structure and occupies a specific volume in space. The approaching of molecules is related to the energy cost associated with the overlap of electron clouds of both these molecules, electrostatic interactions and the appearance of dispersion forces. The problem of this type (encountered in the arenes) was investigated by various researchers [8-10] and is related to the steric effect observed in the theory of reactive collisions used to describe the activation parameters of chemical reactions [11].

2. COMPUTATIONAL PROCEDURES

2.1. Theoretical model

For the complex ethanol-tetracene (E-T) consisting of two subsystems: the molecule of ethanol (E) and the molecule of tetracene (T), the energy of interaction ΔE_{ET} , can be described as a relation:

$$\Delta E_{ET} = E_{ET} - (E_E + E_T) \quad (1)$$

where E_{ET} , E_E and E_T means energy of the complex, energy of subsystem E and energy of subsystem T , respectively. In practical calculations, we use bases with a finite dimension, which leads to a base superposition error (BSSE). Minimizing this error is possible thanks to the counterpoise correction (CP) proposed by Boys and Bernardi [12]. This method requires all calculations to be performed in the same functional basis. The dimer-centred functional basis set (DCBS) of the whole complex is used here, in which both the energy of the complex and its components are taken into account. Therefore, when energy for ethanol is calculated, the functions of the tetracene sub-system, called ghosts functions, are added to its monomer-centred basis set (MCBS). The level of BSSE can be treated as the measure of quantum entanglement of the states of the separate subsystems, *i.e.* the molecule of ethanol and of tetracene.

2.2. Quantum-mechanical calculations

The quantum-mechanical calculations were carried out with use of Gaussian-09 package. The density functional theory (DFT) with use of the B3LYP functional was chosen for calculations. The B3LYP functional was chosen from a literature [13] as an effective tool for calculations of basic states of aromatic hydrocarbons. Due to the complexity of calculations the functional B3LYP/6-31++G(d,p) was used, with diffusion functions for heavy atoms as well as hydrogen atoms. This approach gives a good agreement between the experiment and the calculated energies of orbitals for polycyclic hydrocarbons [14]. The calculations at this level of theory were made to study the variability of the interaction caused when the ethanol molecule come closer to the tetracene molecule. The calculations were carried out for two cases, when the bond of the oxygen atom to the carbon atom in the ethanol molecule is perpendicular to the plane determined by the benzene skeleton of tetracene and when the bond lies in the plane of this skeleton.

3. RESULTS AND DISCUSSION

The quantum mechanical calculations were carried out for the case when the ethanol molecule approaches the tetracene molecule along the line lying in the tetracene skeleton plane. Total energy of the system was corrected by a counterpoise correction (CP), determination of the BSSE energy. The whole energy of the system and the total dipole moment μ were calculated applying the

above mentioned procedure. The results shown in Table 1 apply to the calculation when the oxygen-carbon bond of the ethanol molecule is perpendicular to the tetracene plane, and the results presented in Table 2 concern the case when this bond lies in the tetracene plane. Both of these situations are presented in Fig. 1.

Table 1

The results of approaching the ethanol molecule along the line lying in the plane of tetracene molecule, when the ethanol bond C-O is perpendicular to the tetracene plane

distance d O(ethanol) – C(tetracene) (Å)	4.069	3.873	3.322	2.784
CP corrected energy [eV]	–23081.813	–23081.808	–23081.720	–23081.097
BSSE energy [eV]	$8.19 \cdot 10^{-3}$	$9.81 \cdot 10^{-3}$	$1.65 \cdot 10^{-2}$	$2.76 \cdot 10^{-3}$
Dipole moment μ [D]	2.099	2.120	2.214	2.437

Table 2

The results of approaching the ethanol molecule along the line lying in the plane of tetracene molecule, when the ethanol bond C-O lies in the tetracene plane

distance d O(ethanol) – C(tetracene) [Å]	3.812	3.578	2.952	2.446
CP corrected energy [eV]	–23081,837	–23081,835	–23081,657	–23080,420
BSSE energy [eV]	$8.87 \cdot 10^{-3}$	$1.24 \cdot 10^{-2}$	$2.84 \cdot 10^{-2}$	$4.62 \cdot 10^{-2}$
Dipole moment μ [D]	2.221	2.294	2.725	3.889

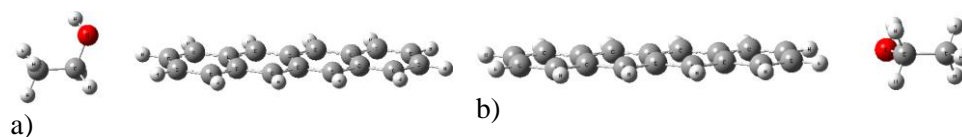


Fig. 1. Schematic images of the two different positions of the C-O bond of ethanol with respect to the plane of tetracene skeleton used in calculations: a) perpendicular, b) in the plane

The BSSE energy as a function of the distance of oxygen of ethanol relative to the corner carbon atom belonging to tetracene for both cases presented in Tables 1 and 2 is shown in Fig. 2. The nature of the relationship indicates that at

the distance less than 3 Å the both dependencies strongly differ. This kind of difference is seen also when we analyse the dependence of BSSE energy in function of the total dipole moment, μ , as shown in Fig. 3.

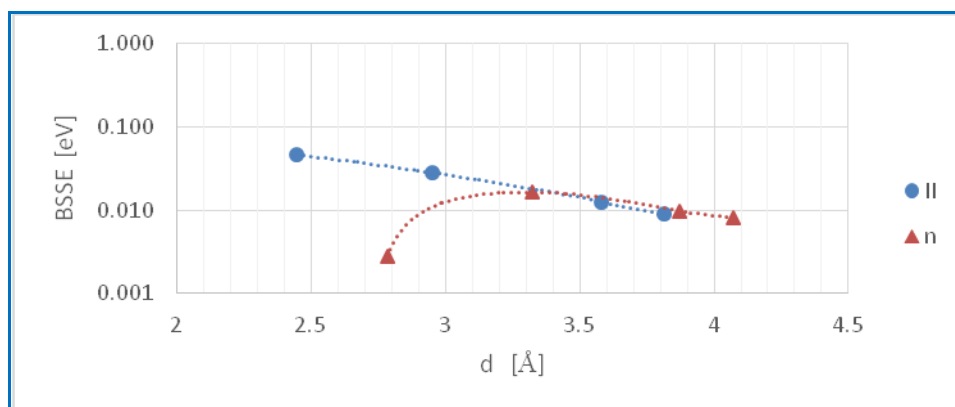


Fig. 2. The BSSE energy as the function of the distance d from the oxygen atom in ethanol molecule to the corner carbon atom in the side benzene ring of tetracene skeleton (n – from Table 1, || – from Table 2). Trend lines are obtained by the least squares method with use of the fourth order polynomial

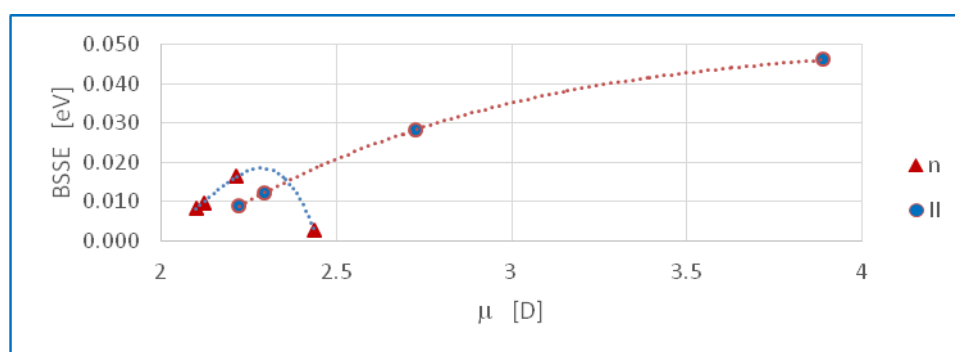


Fig. 3. The BSSE energy as the function of the dipole moment μ of the oxygen atom of the ethanol in respect to the corner carbon atom in the side benzene ring of tetracene skeleton (n – from Table 1, || – from Table 2). Trend lines are obtained by the least squares method with use of the third order polynomial

4. CONCLUSIONS

It is clearly visible that at the distance d less than 3 Å, the BSSE corrections are strongly dependent on the orientation of oxygen carbon bond in ethanol with respect to the tetracene plane (see results in Table 1 and 2, and Fig. 1). The BSSE energy, treated as a measure of quantum entanglement, is 20 times higher for C-O bond of ethanol molecule lying in the tetracene plane than for C-O bond of ethanol molecule perpendicular to the tetracene plane (Fig. 2). This is a circumstantial evidence that the quantum interaction of the ethanol molecule with the tetracene molecule is in the first case about 20 times greater. The dependence between electrostatic interactions, seen as an induced total dipole moment and quantum entanglement seen as BSSE energy, presented in Fig. 3, is different in two studied cases. The above suggests that we are dealing with a steric effect applied in the theory of active collisions in the adsorption reactions [11]. This also means that the nature of the collisions of the ethanol molecule with tetracene molecule is different for the above mentioned cases of orientation of the C-O bond belonging to methanol with respect to the tetracene plane (see Fig. 1). We can assess that the translational component of the ethanol molecule conserves to a large extent during active collisions in the case of setting the C-O bond of ethanol perpendicular to the tetracene plane (Fig. 1a). If that bond lies in the tetracene plane (Fig. 1b), the interaction should favour the oscillation of the ethanol molecule. Thus, the problem of an organic sensor based on tetracene requires further studies applying quantum mechanical calculations.

ACKNOWLEDGEMENTS

The results of quantum-mechanical calculations presented in this paper applied Gaussian-09 package implemented in the PLATON project infrastructure in the Computer Centre of the Lodz University of Technology.

REFERENCES

- [1] Yunusa Z., Hamidon M.N., Kaiser A., Awang Z. 2014. Gas sensors: a review. *Sensors & Transducers*. 68: 61-75.
- [2] Boukhili W., Mahdouani M., Erouel M., Puigdollers J., Bourguiga R. 2015. Reversibility of humidity effects in pentacene based organic thin-film transistor: Experimental data and electrical modeling. *Synt. Met.* 199: 303-309.
- [3] Kania S., Kuliński J. 2011. Activation of thin layers of two aromatic hydrocarbons. *Chem. Met. Alloys* 4: 31-37.

- [4] Kania S., Kuliński J. 2012. Conductivity due to the active collisions channel of absorption of ethanol to thin layers of acenes. *Sci. Bull. Techn, Univ.Lodz, Physics*, 33: 65-72.
- [5] Mao H., Guan D., Chen M., Dou W., Song F., Zhang H., Li H., He P., Bao S. 2009. The chemisorption of tetracene on Si(100)-2×1 surface. *J. Chem. Phys.* 131: 044703-1 – 044703-5.
- [6] Liu S-S., Bian L-J., Luan F., Sum M-T., Liu X-X. 2012. Theoretical study on polyaniline gas sensors: Examinations of response mechanism for alcohol. *Synth. Met.* 162: 862-867.
- [7] Migliore A., Naaman R., and Beratan D. N. 2015. Sensing of molecules using quantum dynamics. *Proc. Natl. Acad. Sci. USA* 112: E2419-E2428.
- [8] Oliveira B.G., Vasconcellos M.L.A.A, Olinda R.R., Filho E.B.A. 2009. Uncommon hydrogen bonds between a non-classical ethyl cation and π hydrocarbons: a preliminary study. *Struct. Chem.* 20: 81-90.
- [9] Kumbhar S., Fischer F.D., Waller M.P. 2011. Assessment of weak intermolecular interactions across QM/MM noncovalent boundaries. *J. Chem. Inf. Model.* 52: 93-98.
- [10] Levitt M., Perutz M.F. 1988. Aromatic rings act as hydrogen bond acceptors. *J. Mol. Biol.* 201: 751-754.
- [11] Atkins P.W., de Paula J. 2014. *Atkins' physical chemistry*, Oxford, University Press.
- [12] Boys S.F., Bernardi F. 1970. The calculation of small molecular interactions by the differences of separate total energies. Some procedures with reduced errors. *Mol. Phys.* 19: 553-566.
- [13] Mallocci G., Cappellini G., Mulas G., Mattoni A. 2011. Electronic and optical properties of families of polycyclic aromatic hydrocarbons: a systematic (time-dependent) density functional theory study. *Chem. Physics* 384: 19-27.
- [14] Coropceanu V., Cornil J., da Silva Filho D.A., Olivier Y., Silbey R., Bredas J.-L. 2007. Charge Transport in Organic Semiconductors. *Chem. Rev.* 107: 926-952.

SENSORYCZNOŚĆ WARSTW TETRACENU JAKO WYNIK SPLĄTANIA KWANTOWEGO

Streszczenie

Zastosowanie metod obliczeń kwantowo-mechanicznych umożliwiło badanie zmienności oddziaływań pomiędzy cząsteczkami etanolu i tetracenu. Obecność splątania kwantowego stanów kwantowych widziana jest podczas obliczeń na dwa sposoby – jako zmiana momentu dipolowego i jako narastanie błędu superpozycji bazy (BSSE), gdy odległość między badanymi cząsteczkami maleje. Obserwowane są zależności całkowitej energii układu zależnie od chwilowego wzajemnego ustawienia długich osi cząsteczek, jak też i orientacji wiązania atomu tlenu z węglem w etanolu względem płaszczyzny szkieletu benzenowego cząsteczki tetracenu.

**PAULINA KOMAR¹, PATRYCJA ŚPIEWAK¹,
MARCIN GĘBSKI^{1,2}, JAMES A. LOTT², MICHAŁ WASIAK¹**

¹Institute of Physics, Lodz University of Technology, ul. Wólczńska 219,
90-924 Łódź, Poland, e-mail: paulina.komar@p.lodz.pl

²Institute of Solid State Physics and the Center of Nanophotonics,
Technical University of Berlin, D-10632 Berlin, Germany

CURRENT DEPENDENCE OF RESISTANCES AND CAPACITANCES IN A VERTICAL-CAVITY SURFACE-EMITTING LASER

Based on the model of impedance and modulation time constants for vertical-cavity surface-emitting lasers (VCSELs) we study the resistances and capacitances of an equivalent circuit as a function of the current flowing through the VCSEL. We observe reduction of some components of the resistance and the capacitance, as well as the modulation time constants for increasing current.

Keywords: VCSEL, high-frequency modulation, capacitance, modelling of semiconductor lasers.

1. INTRODUCTION

In recent years, the vertical-cavity surface-emitting lasers (VCSELs) are constantly gaining importance as transmitters in short-range optical data transfer due to their low cost, small size, low power consumption, and good quality of the emitted beam [1-3]. While being used as the light source for optical data communication, the VCSEL is set at a fixed bias current and modulated with a high-frequency voltage. At the modulation frequencies of tens of GHz, enabling high bandwidth data transmission, it becomes important to identify and investigate how the electrical capacitances and resistances present in the system depend on operation parameters of a laser to assure error-free operation [4-5].

2. SIMULATION MODEL

The simulations of the temperature and electrical potential distributions inside semiconductor lasers are performed based on the self-consistent thermal-electrical model developed by the Photonics Group at the Lodz University of Technology [6-7]. The investigations presented in this article are based in particular on an extension of this model, *i.e.* the numerical model of impedance developed by Wasiak *et al.* [5]. The main idea of this model is a division of the entire laser into areas whose borders have the same potential. Knowing the equipotential surfaces one can connect these areas in series while building an equivalent circuit.

A scheme of the investigated laser and its equivalent electrical circuit are presented in Fig. 1(a) and 1(b), respectively. The VCSEL structure consists of a p-type and n-type distributed Bragg reflectors (DBRs), spaced by a p-i-n junction (drawn in green), *i.e.* the undoped material between two doped semiconductors. We consider also two oxide layers – one on the p-type side (drawn in purple) and one on the n-type side (drawn in blue) of the junction. As one can find equipotential surfaces between these layers, one can create an equivalent circuit composed of capacitances (C) and resistances (R) due to oxide layer on the p-type side (with subscript oxp), due to junction layer (with subscript j), and due to oxide layer on the n-type side (with subscript oxn).

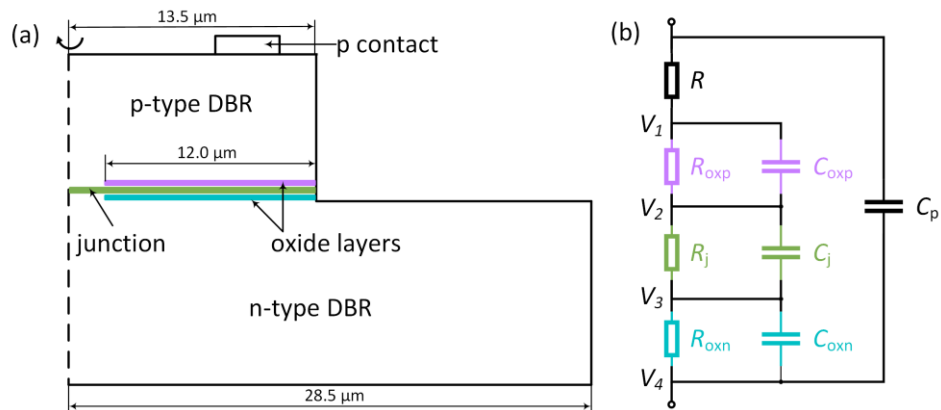


Fig. 1. (a) A scheme of the VCSEL structure employed to simulations. The thicknesses of the oxide layers and the active region (junction) are not drawn to scale. (b) An equivalent circuit of a VCSEL with oxide layers on both sides of a junction. Description of symbols is given in the text

The resistance of the remaining semiconductor material is labelled with R , whereas the capacitance of the insulating materials surrounding the laser is represented by C_p .

It is crucial to mention that the physical borders between the layers (*e.g.* the oxide layer on the p-type side and the junction) do not overlap with the equipotential surfaces that are used for definition of the equivalent circuit. One can clearly see this situation on maps presented in Fig. 2, where the equipotential lines are drawn in black on top of the VCSEL zoomed on the active region (yellow) and the oxide layers located on its both sides (purple). Thus, area that is located between potentials V_1 and V_2 (compare Figs. 1(b) and 2) is considered as the resistance R_{oxp} and capacitance C_{oxp} , between potentials V_2 and V_3 corresponds to the junction (R_j and C_j), whereas between V_3 and V_4 is treated as the resistance R_{oxn} and capacitance C_{oxn} due to oxide layer on the n-type side.

3. SIMULATION RESULTS

The simulations were performed for a structure [1-3] schematically presented in Fig. 1(a), for which the aperture diameter is equal to 3 μm , the diameter of the p-type DBR is equal to 27 μm , and the diameter of the n-type DBR is equal to 57 μm . The numerical studies of the temperature and potential distributions were executed for four fixed values of voltage ($U = 1.9, 2.1, 2.5, 3.0$ V) applied to the contacts of the laser. The performed calculations allowed for determination of the values of the current flowing through the VCSEL, all the resistances and capacitances in the model, and the maximum value of the modulation time constant.

The values of the resistances calculated as a function of the current flowing through the VCSEL are presented in Fig. 3. Due to the fact that R_j is the differential resistance of the junction, one can observe a strong decrease of its value as a function of current. In contrast, R_{oxn} and R are almost independent on I . The highest values of the resistance were obtained for oxidation layer on the p-type side due to lower electrical conductivity of p-type semiconductors used for construction of the DBR. The total resistance (sum of all discussed resistances) of the VCSEL as well as the R_{oxp} are decreasing for increasing current, what is in agreement with experimental observations [1].

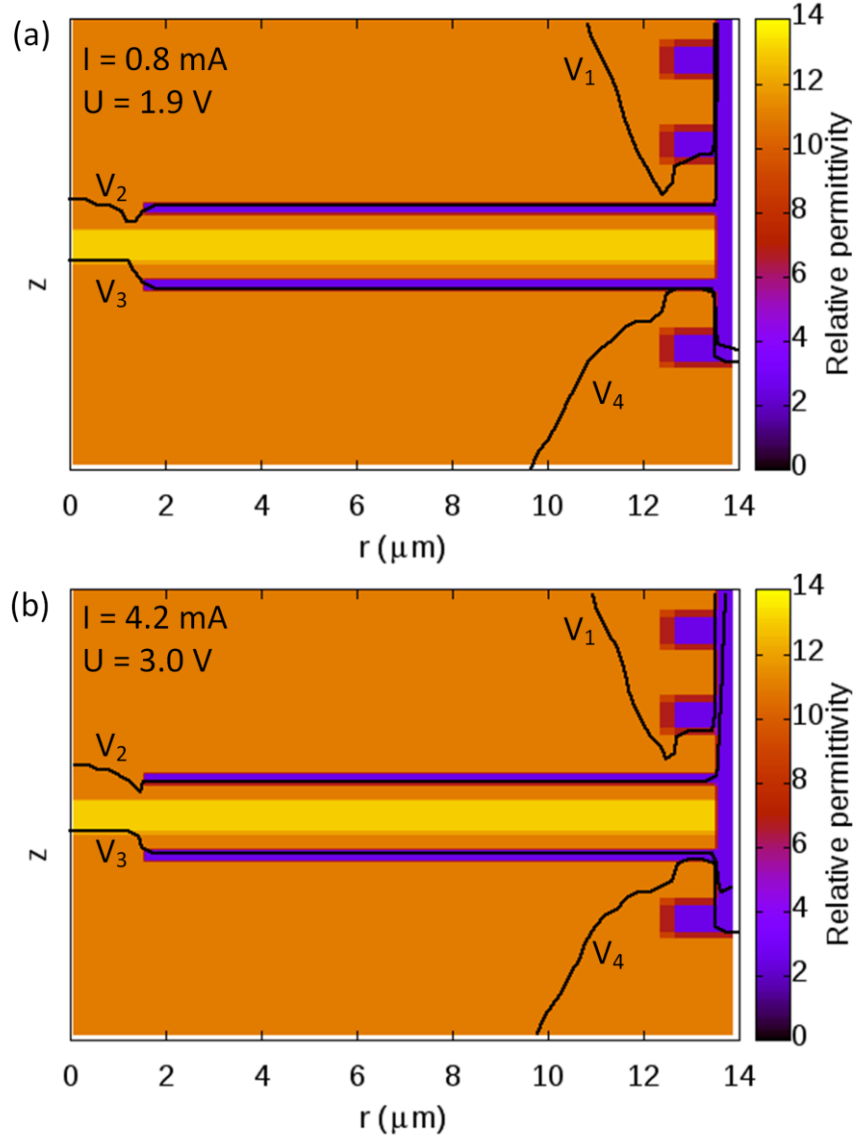


Fig. 2. The equipotential lines drawn on top of the VCSEL structure for (a) current $I = 0.8 \text{ mA}$, voltage $U = 1.9 \text{ V}$ and (b) current $I = 4.2 \text{ mA}$, voltage $U = 3.0 \text{ V}$. Individual layers may be distinguished based on their relative permittivity. The maps show a zoom on the active region and the oxide layers located on its both sides

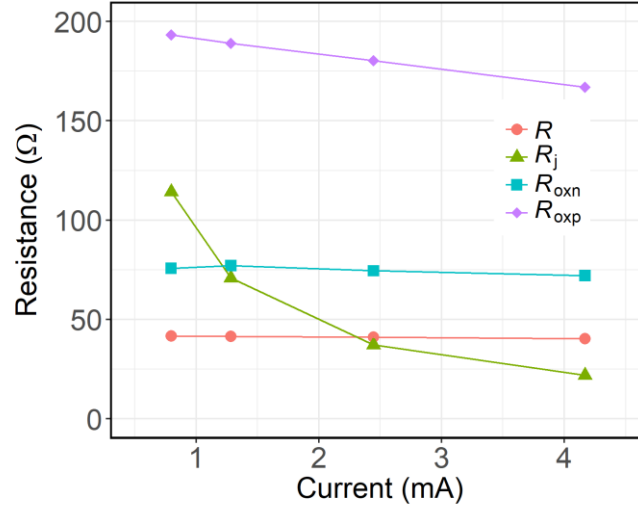


Fig. 3. Calculated values of resistances present in an equivalent circuit as a function of the current flowing through the VCSEL. The lines are guides to the eye

The calculated values of capacitances as a function of the current are shown in Fig. 4. The capacitances of the junction C_j and the dielectric material surrounding the laser C_p are almost independent on the current. On the other hand, one can notice significant decrease of the capacitances due to oxide layers. That is due to the fact that change of the applied voltage leads to a change of the distribution of the potentials $V_1 - V_4$. For higher voltage (see Fig. 2(b)), the potentials V_2 and V_3 move towards the junction as compared to the lower voltage (see Fig. 2(a)). Therefore, the effective oxidation thickness increases for increasing voltage (and also the current), what leads to the decrease of the capacitance.

Based on the employed model of capacitance one can also calculate the modulation time constants τ . In Fig. 5, we present the maximum value of τ from among three calculated time constants. As clearly visible, the value of the modulation time constant decreases for increasing current. Therefore, for higher current the VCSEL may be modulated with higher frequency enabling quicker data transfer.

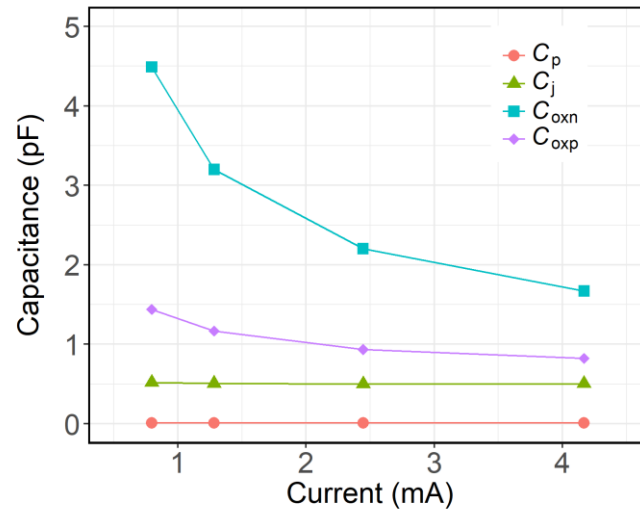


Fig. 4. Calculated values of capacitances present in an equivalent circuit as a function of the current flowing through the VCSEL. The lines are guides to the eye

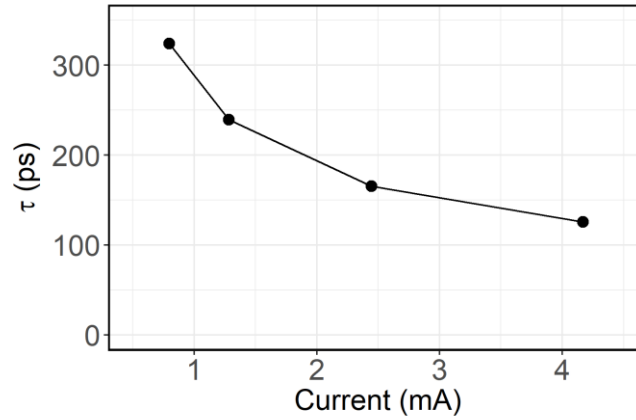


Fig. 5. Modulation time constant as a function of the current flowing through the VCSEL. The line is a guide to the eye

4. CONCLUSIONS

Employing the model of impedance for VCSELs we have calculated the resistances and capacitances of a laser as a function of the current. We observe that the differential resistance as well as capacitances associated with the oxide layers are decreasing for increasing current. That leads to a decrease of modulation time constant for increasing I , enabling modulation with higher frequency and faster data transfer.

ACKNOWLEDGMENT

We gratefully acknowledge financial support by NCN 2016/21/B/ST7/03532.

REFERENCES

- [1] Li H., Lott J.A., Wolf P., Moser P., Larisch G., Bimberg D. 2015. Temperature-dependent impedance characteristics of temperature-stable high-speed 980 nm VCSELs. *IEEE Photon. Technol. Lett.* 27:832-835.
- [2] Li H., Wolf P., Moser P., Larisch G., Lott J.A., Bimberg D. 2014. Temperature-stable 980 nm VCSELs for 35 Gb s⁻¹ operation at 85 °C with 139 fJ/bit dissipated heat. *IEEE Photon. Technol. Lett.* 26:2349-2352.
- [3] Moser P., Lott J.A., Larisch G., Bimberg D. 2015. Impact of the oxide-aperture diameter on the energy-efficiency, bandwidth, and temperature stability of 980 nm VCSELs. *J. Lightwave Technol.* 33:825-831.
- [4] Ou Y., Gustavsson J.S., Westbergh P., Haglund Å., Larsson A., Joel A. 2009. Impedance characteristics and parasitic speed limitations of high-speed 850 nm VCSELs. *IEEE Photon. Technol. Lett.* 21:1840-1842.
- [5] Wasiak M., Śpiwak P., Moser P., Walczak J., Sarzała R.P., Czyszanowski T., Lott J.A. 2016. Numerical model of capacitance in vertical-cavity surface-emitting lasers. *J. Phys. D: Appl. Phys.* 49:175104.
- [6] Piskorski Ł., Sarzała R.P., Nakwaski W. 2007. Self-consistent model of 650 nm GaInP/AlGaInP quantum-well vertical-cavity surface-emitting diode lasers. *Semicond. Sci. Technol.* 22:593-600.
- [7] Xu D., Tong C., Yoon S.F., Fan W., Zhang D.H., Wasiak M., Piskorski Ł., Gutowski K., Sarzała R.P., Nakwaski W. 2009. Room-temperature continuous-wave operation of the In(Ga)As/GaAs quantum-dot VCSELs for the 1.3 μm optical-fibre communication. *Semicond. Sci. Technol.* 24:055003.

PRĄDOWA ZALEŻNOŚĆ REZYSTANCJI I POJEMNOŚCI W LASERZE O EMISJI POWIERZCHNIOWEJ Z PIONOWĄ WNĘKĄ REZONANSOWĄ

Streszczenie

W oparciu o model impedancji i stałych czasowych modulacji dla laserów o emisji powierzchniowej z pionową wnęką rezonansową (VCSEL) badamy opory i pojemności równoważnego obwodu w funkcji prądu przepływającego przez laser. Obserwujemy, że wraz ze wzrostem prądu przepływającego przez urządzenie, niektóre ze składowych rezystancji i pojemności w elektrycznym układzie zastępczym ulegają zmniejszeniu. Wraz ze wzrostem prądu zmniejsza się również stała czasu modulacji.

**MAGDALENA MARCINIAK^{1,2}, MARCIN GĘBSKI^{1,2},
MACIEJ DEMS¹, TOMASZ CZYSZANOWSKI¹**

¹Institute of Physics, Lodz University of Technology, ul. Wólczńska 219,
90-924 Łódź, Poland, e-mail: magdalena.marciniak@p.lodz.pl

²Institute of Solid State Physics and Center of Nanophotonics, Technische
Universität Berlin, Hardenbergstraße 36, D-10623 Berlin, Germany

SUBWAVELENGTH HIGH CONTRAST GRATINGS AS OPTICAL SENSING ELEMENTS

Subwavelength high contrast gratings (HCG) can be used as high reflective mirrors and can be used as mirrors of vertical-cavity surface-emitting lasers. HCG mirrors can be designed in such a way that they are extremely sensitive to environmental changes - changes in the refractive index of ambient substance or changes in the absorption coefficient may cause changes in mirror reflectivity. This phenomenon can be used to detect liquids and gases. In this paper we present analysis of HCG properties. We consider the various HCG mirror designs and the possibilities of detecting gases and liquids.

Keywords: Vertical-Cavity Surface-Emitting Lasers (VCSELs), Optical sensors, subwavelength gratings.

1. INTRODUCTION

Subwavelength High Contrast Gratings (HCGs) found many applications in various areas of integrated photonic. They can be used e.g. as focusing lenses and reflectors or high-quality-factor optical resonators [1] but the most promising application for HCG is to use them as the top mirror in Vertical-Cavity Surface-Emitting Lasers (VCSELs) in place of conventionally used Distributed Bragg Reflectors (DBRs) [2-5]. HCGs are diffraction gratings with subwavelength spatial dimensions. They should be made of material with refractive index much higher than surroundings. Properly designed HCGs provide very high (close to unity) power reflectance or transmission in wide range of wavelength. They also provide high discrimination of polarization of incident light. HCGs can be made in different ways: as a grating located on

cladding layer (usually made of dielectric) [2], as a membrane suspended in the air [4-7] or as monolithic HCG (MHCG) [8, 9] (see Fig. 1).

HCGs provide very high power reflectance in wide range of wavelength, in general wider than MHCGs. However their construction requires layer of dielectric material or air gap, which is main drawback of HCGs as mirrors in VCSELs. MHCGs can be made of any kind of semiconductor material of refractive index higher than 1.75 [8, 9], but their power reflectance spectrum is narrower, but still comparable with DBR's spectrum. Some constructions of HCGs or MHCGs can be very sensitive to properties of surrounding medium, especially to absorption or refractive index changes. We can use that property to design new type of detectors with HCGs. In this paper we show how sensitive can be HCGs and MHCGs to changes in surrounding medium. Based on numerical calculations we present constructions of HCGs and MHCGs which can be used as optical sensors. We analyse the influence of absorption and refractive index of surrounding for power reflectance and other optical properties of mirror.

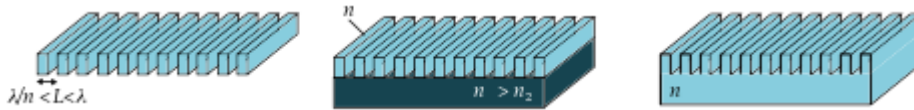


Fig. 1. Different construction of HCG mirrors: membrane suspended in the air (left), grating put on a cladding layer (center) and monolithic HCG (right)

Since now there were proposals to use subwavelength structures for detection. In [10] authors showed, how to use HCG resonator for liquid sensing. However we propose to employ as a sensor whole VCSEL with HCG mirror, which is new approach.

2. COMPUTER MODEL

For our study we use three dimensional, fully vectorial model. We consider single period with periodic boundary condition. To perform our calculations we employ plane-wave admittance method (PWAM) [11]. PWAM converts the problem of solving the set of differential equations into the problem of finding eigenvalues of a matrix. It solves Maxwell equations with only assumption on planar structure in a frequency domain by using a plane-wave expansion within each layer and computes an analytical solution in the perpendicular direction. Such approach is possible due to transformation of the electromagnetic field to the diagonal coordinates which makes algorithm very time and memory

efficient. The boundary conditions can be imposed in the form of the propagating wave in the direction of the analytical solution and as Perfectly Matched Layer (PML) being absorbing condition or periodic boundary condition in the plane of plane-wave expansion.

Agreement between experimental data and our computer model for MHCGs mirror is confirmed in [9].

In this paper, we took into consideration mirrors designed for wavelength $\lambda = 1.651 \mu\text{m}$ which corresponds to the peak of methane absorption spectrum [12]. However similar devices can be designed for arbitrary wavelength and find application in many of sensing applications. We perform our calculations for MHCG mirror made of InP and for Si HCG implemented on SiO_2 cladding layer. Materials parameters used in our calculations are set in Table 1.

To describe HCGs or MHCGs we can use following parameters (see Fig. 2): period of the structure L , width of the stripe a , height of the stripe h , thickness of cladding layer h_c and fill factor F , which is the ratio of width of the stripe and period of the structure. To find optimal parameters of the mirror

Table 1

Material parameters used for calculations– values of refractive indices n of different materials for $\lambda = 1.651 \mu\text{m}$

material	InP [13]	Si [14]	SiO2 [15]
n	3.15	3.47	1.46

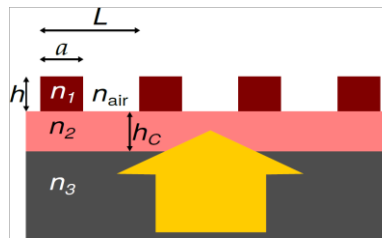


Fig. 2. Schematic structure of HCG mirror; L – period of grating, a – width of stripe, h – high of stripe, h_c – high of cladding layer, n_1 , n_2 , n_3 – refractive indices of materials, n_{air} – refractive index of surrounding medium. For MHCG mirror $n_1 = n_2 = n_3$

(which provide the highest possible power reflectance) we should consider the power reflectance as a function of spatial parameters of the grating (L , F and h) and perform three dimensional optimization of the power reflectance. In case of sensing elements high power reflectance is not enough. We should find structures for which power reflectance differs significantly for variable external conditions.

3. GAS DETECTION

Presence of gas around the stripes can influence the power reflectance of HCGs and MHCGs. For most of gases refractive index is very close to the unity, which corresponds with refractive index of air. Because of that, it is very hard to detect gases based on refractive index changes. However every gas has very characteristic absorption spectrum, which makes them easy to detect by measurement of absorption coefficient. In this part we would like to show dependence between absorption coefficient of grating surrounding and grating power reflectance.

In Fig. 3 one can see power reflectance maps for MHCGs mirrors for TE and TM polarization. In this figures, we present power reflectance R as a function of L and h for given fill factor F for transverse electric (TE) and transverse magnetic (TM) polarization of incident light with wavelength $\lambda = 1.65 \mu\text{m}$. The figures also illustrate difference of power reflectance for absorption coefficient of surroundings equal to $\alpha = 0 \text{ cm}^{-1}$ and $\alpha = 0.05 \text{ cm}^{-1}$, which is absorption coefficient for 100% methane concentration at $\lambda = 1.65 \mu\text{m}$. We consider MHCGs, based our preliminary studies which shows, that they are much more sensitive to absorption coefficient changes than HCGs. Based on data presented in Fig. 3 we found different structures that provide high power reflectance and high difference of power reflectance for absorption changes at the same time. Parameters of such mirrors are set in Table 2.

Table 2

Parameters of MHCG mirrors which can be used for gas detections

polarization	L [nm]	F	h [nm]	$R (\alpha = 0)$	$dR/d\alpha$ [cm]
TE	977	0.475	2240	$1 - 6 \cdot 10^{-4}$	$- 2.3 \cdot 10^{-3}$
TM	958	0.693	2441	$1 - 10^{-6}$	$- 3.8 \cdot 10^{-4}$

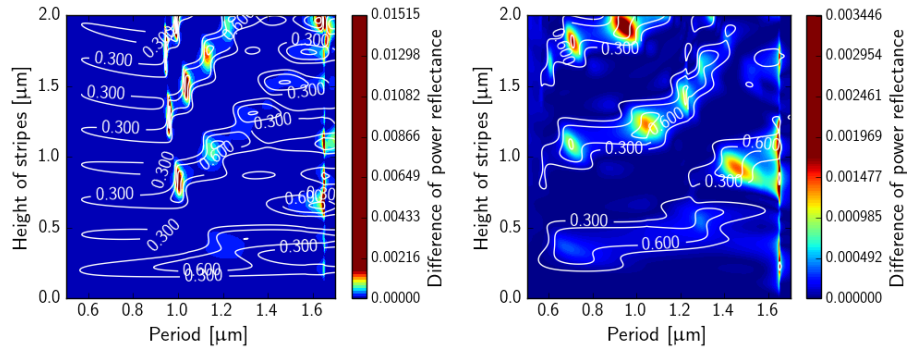


Fig. 3. Difference of power reflectance for absorption coefficient of surroundings equal to $\alpha = 0 \text{ cm}^{-1}$ and $\alpha = 0.05 \text{ cm}^{-1}$ as a function of height of stripes h and period of grating L for fill factor $F = 0.5$ for TE polarization and $F = 0.7$ for TM polarization. The results were obtained for MHCG mirror for TE (left) and TM (right) polarization of incident light with wavelength $\lambda = 1.65 \text{ μm}$. White solid lines indicate values of power reflectance for $\alpha = 0 \text{ cm}^{-1}$

4. LIQUID DETECTION

Based on that properties of HCGs and MHCGs, they can be also used for liquid detection. Variable liquids are characterized by different values of refractive index. Refractive index of liquid can strongly depends on external factors, e.g. temperature or chemical composition. Because of that we observe refractive index changes to characterize liquids. Same as the case of gas, presence of liquid between stripes also influences on optical properties of mirror, especially on power reflectance. In Figs. 4 and 5 one can see power reflectance as a function of spatial parameters of HCGs and MHCGs respectively. Figures 4 and 5 illustrate the power reflectance R for TE and TM polarization of incident light with wavelength $\lambda = 1.65 \text{ μm}$. Figures 4 and 5 also illustrate difference of power reflectance for refractive index of surroundings equal to $n_l = 1.0$ and $n_l = 1.1$, which is hypothetical value not related to any specific liquid. However this range of refractive index changes should be useful for detection.

Based on data presented in Figs. 4 and 5 we found four different structures that provide high power reflectance and high difference of power reflectance for refractive index changes at the same time. Parameters of such mirrors are given in Tables 3 (for HCG mirrors) and 4 (for MHCG mirrors). Changes of the refractive index of surroundings medium influence on the optical field distribution in HCGs and MHCGs, which can be seen in Fig. 6. In this case

changes in optical field distribution are more noticeable than in the case of absorption changes.

Table 3

Parameters of HCG mirrors which can be used for liquid detections

polarization	L [nm]	F	h [nm]	$R(\alpha = 0)$	$dR/d\alpha$ [cm]
TE	1616	0.415	1255	$1 - 4 \cdot 10^{-4}$	$-1.55 \cdot 10^{-3}$
TM	1361	0.201	2020	$1 - 10^{-5}$	$-7.48 \cdot 10^{-4}$

Table 4

Parameters of MHCG mirrors which can be used for liquid detections

polarization	L [nm]	F	h [nm]	$\underline{R}(\alpha = 0)$
TE	1515	0.387	2227	$1 - 6 \cdot 10^{-4}$
TM	1114	0.396	838	$1 - 10^{-5}$

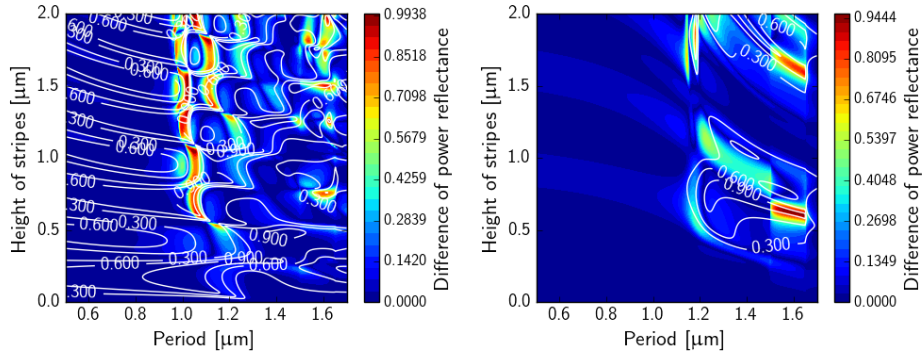


Fig. 4. Difference of power reflectance for refractive index of surroundings equal to $n_l = 1.0$ and $n_l = 1.1$ as a function of height of stripes h and period of grating L for fill factor $F = 0.4$ for TE polarization and $F = 0.2$ for TM polarization. The results were obtained for HCG mirror for TE (left) and TM (right) polarization of incident light with wavelength $\lambda = 1.65 \mu\text{m}$. White solid lines indicate values of power reflectance for $n_l = 1.0$

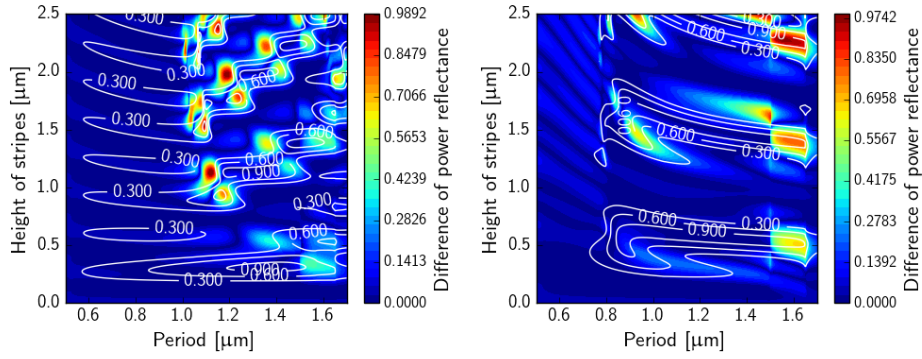


Fig. 5. Difference of power reflectance for refractive index of surroundings equal to $n_l = 1.0$ and $n_l = 1.1$ as a function of height of stripes h and period of grating L for fill factor $F = 0.4$. The results were obtained for MHCG mirror for TE (left) and TM (right) polarization of incident light with wavelength $\lambda = 1.65 \mu\text{m}$. White solid lines indicate values of power reflectance for $n_l = 1.0$

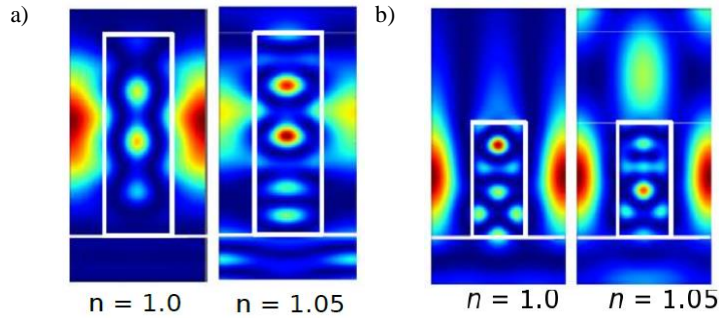


Fig. 6. Optical field distribution in stripes of HCG (a) and MHCG (b) mirrors for TE polarization

5. APPLICATION IN VCSELS

Based on presented results one can notice that HCGs and MHCGs can be very sensitive to changes of surrounding medium. Even small change of absorption or refractive index influence on power reflectance. This phenomena can be used to detect gases or liquids. For that we can employ VCSELS designed for specific wavelength *e.g.* for methane detection we design 1651 nm InP-based VCSEL. The idea of such detectors is following: presence of gas or liquid between stripes influences power reflectance of top mirror and, consequently,

the electric properties of VCSELs. By this the voltage-current characteristic is changed. Hence one can deduce information on surrounding of grating by observation of voltage-current characteristic.

One can notice that such devices would be more sensitive for refractive index changes than for absorption coefficient changes, which makes such detectors better for liquid sensing. Such devices can be used not only for liquid detection, but also for studying optical properties of liquids.

The most important advantage of that solution is that one can be able to design detector which requires only one element, which is laser. Usually optical sensing systems employ light source and external detector. In proposed design only the light-emitting device is required.

6. SUMMARY

In conclusion, we presented analysis of properties of HCGs and MHCGs mirrors as sensing elements. We showed that HCGs and MHCGs can be very sensitive to changes of refractive index or absorption of surrounding medium. We performed our analysis based on mirrors designed for 1651 nm wavelength, which corresponds to the maximum of the methane absorption. However HCGs or MHCGs can be designed for another wavelength of incident light [9], which can enable to detect another substances.

REFERENCES

- [1] Chang-Hasnain C.J., Yang W. 2012. High-contrast gratings for integrated optoelectronics. *Adv. Opt. Photonics* 4: 379-440.
- [2] Chung I-S, Mork J., Gilet P., Cheikonov A. 2008. Subwavelength grating-mirror VCSEL with a thin oxide gap. *IEEE Photon. Technol. Lett.* 20: 105-107.
- [3] Sciancalepore C., Ben Bakir B., Letartre X., Fedeli J.-M., Olivier N., Bordel D., Seassal C., Rojo-Romeo P., Regreny P., Viktorovitch P. 2011. Quasi-3D light confinement in double photonic crystal reflectors VCSELs for CMOS-compatible integration. *IEEE J. Lightwave Technology* 29: 2015-2024.
- [4] Huang M.C.Y., Zhou Y., Chang-Hasnain C.J. 2007. Surface emitting laser incorporating a high-index-contrast subwavelength grating. *Nat. Photonics* 1: 119-122.
- [5] Chase C., Rao Y., Hoffmann W., Chang-Hasnain C.J. 2010. 1550 nm high contrast grating VCSEL. *Opt. Express* 18: 15461-15466.
- [6] Hashemi E., Bengtsson J., Gustavsson J.S., Carlsson S. 2015. TiO₂ membrane high-contrast grating reflectors for vertical-cavity light-emitters in the visible wavelength regime. *J. Vac. Sci. Technol. B* 33: 050603.

-
- [7] Wu T.S. Wu T.T., Syu Y.C., Wu S.H., Chen W.T., Lu T.C., Wang S.C., Chiang H.P., Tsai D.P. 2012. Sub-wavelength GaN-based membrane high contrast grating reflectors. *Opt. Express* 20: 20551-20557.
 - [8] Gębski M., Dems M., Szerling A., Motyka M., Marona L., Kruszka R., Urbańczyk D., Walczakowski M., Pałka N., Wójcik-Jedlińska A., Wang Q.J., Zhang D.H., Bugajski M., Wasiak M., Czyszanowski T. 2015. Monolithic high-index contrast grating: a material independent high-reflectance VCSEL mirror. *Opt. Express* 23: 11674-11686.
 - [9] Marciniak M., Gębski M., Dems M., Haglund E., Larsson A., Riazat M., Lott J.A., Czyszanowski T. 2016. Optimal parameters of monolithic high-contrast grating mirrors. *Optics letters*. 41: 3495-3498.
 - [10] Karagodsky V., Tran T., Wu M., Chanh-Hasnain C. 2011. Double-Resonant Enhancement of Surface Enhanced Raman Scattering Using High Contrast Grating Resonators. *CLEO: 2011 – Laser Applications to Photonic Applications*.
 - [11] Dems M., Kotyński R., Panajotov K. 2005. Plane Wave Admittance Method – a novel approach for determining the electromagnetic modes in photonic structures. *Opt. Express* 13: 3196-3207.
 - [12] Hodgkinson J., Tatam R.P. 2013. *Meas. Sci. Technol.* Optical gas sensing: a review. 24: 012004.
 - [13] Pettit G.D., Turner W.J. 1965. Refractive Index of InP. *J. App. Phys.* 36: 2081.
 - [14] Li H.H. 1980. Refractive index of silicon and germanium and its wavelength and temperature derivatives. *J.Phys. and Chem. Reference data* 9: 561.
 - [15] Gao L., Lemarchand F., Lequime M. 2012. Exploitation of multiple incidences spectrometric measurements for thin film reverse engineering. *Opt. Express* 20: 15734.

PODFALOWE SIATKI DYFRAKCYJNE O WYSOKIM KONTRAŚCIE WSPÓŁCZYNNIKA ZAŁAMANIA ŚWIATŁA JAKO SENSORY OPTYCZNE

Streszczenie

Zwierciadła HCG to podfalowe siatki dyfrakcyjne wykonane z materiału o wysokim współczynniku załamania światła. Mogą one zostać wykorzystane jako zwierciadła o wysokiej odbijalności w laserach typu VCSEL. Zwierciadła HCG można zaprojektować w taki sposób, że będą wyjątkowo czułe na zmiany współczynnika załamania światła lub współczynnika absorpcji w otoczeniu zwierciadła. Zmiana tych parametrów powoduje zmianę odbijalności zwierciadła HCG. Zjawisko to może być wykorzystane w sensorach optycznych. W niniejszej pracy prezentujemy analizę właściwości zwierciadeł HCG. Rozważamy różne struktury zwierciadeł HCG i pokazujemy, że mogą być one wykorzystane do detekcji gazów i cieczy.

**MARTA WIĘCKOWSKA, MACIEJ DEMS,
TOMASZ CZYSZANOWSKI**

Institute of Physics, Lodz University of Technology, ul. Wólczńska 219,
90-924 Łódź, Poland

COMPARISON OF METHODS FOR SIMULATION OF THE OPTICAL PROPERTIES OF VCSELs

This paper presents the differences arising from the use of scalar (Effective Frequency Method) and vector (Fourier's and Bessel's Admittance Methods) calculation methods in optical analysis of arsenide Vertical-Cavity Surface-Emitting Lasers (VCSELs). Discussed results demonstrate that the vector methods are more accurate than the scalar one, but also they are more time consuming. By comparing two vector methods, it can be seen that the Bessel's Admittance Method allows to obtain similar qualitatively and quantitatively results in a slightly shorter time. The calculations were performed for structures with varied aperture radius and its location in the resonant cavity. Moreover, this paper includes the comparison of calculation results for a structure in which there are layers with gradually changing refractive index, and the structure in which these layers are replaced by a layer with a constant average refractive index.

Keywords: modelling of semiconductor devices, semiconductor lasers, vertical-cavity surface-emitting laser (VCSEL).

1. INTRODUCTION

Today, semiconductor lasers are used in many different areas of everyday life. An important class of such lasers consists of Vertical-Cavity Surface-Emitting Lasers (VCSELs), which have very good beam parameters and provide low cost of mass production. Because of their advantages, these lasers are becoming more and more popular among physicists, technologists and entrepreneurs. As a result, there is a demand for their accurate modelling in order to design the new generations of VCSELs [6]. The simulation methods include

optical, electrical and thermal models, which all together can give almost full view on the VCSEL's properties. Optical models are expected to determine several points, such as modal losses and gain, wavelength of emitted radiation or intensity profile [4]. At the same time, this modelling process should be performed within computational resources and time. Hence, the choice of the most appropriate computational method becomes an important issue [7].

In this paper we present three of such computational methods: the scalar Effective Frequency Method (EFM) [1], the vector Fourier's Admittance Method [2], and the vector Bessel's Admittance Method [3]. We compare these methods by presenting the dependence of the wavelength and the photon lifetime on the size of the VCSEL oxide aperture. We also show the average time of calculation of each method, to investigate the applicability of each of these methods for VCSEL analysis. As both the accuracy and the numerical effort of the vector methods depend on the size of expansion basis, we also analyze the convergence of these methods for increasing basis size.

2. COMPUTATIONAL METHODS

In the first step of our analysis we compare the computational methods. These methods are: the Effective Frequency Method (EFM), which is an example of a scalar model, and two vector admittance methods: Bessel and Fourier. Below, the main assumptions and the main differences between them are shown.

2.1. Effective Frequency Method

The Effective Frequency Method [1][5] is one of the scalar computational methods. It is assumed that the optical field is linearly polarized in the fixed direction throughout the analyzed structure and that in a VCSEL laser it can be divided into factors, each of which depends on one variable:

$$E(r, z, \varphi) = E_{r,z}(r, z) E_r(r) \exp(iL\varphi) \quad (1)$$

where $L = 0, 1, 2, \dots$ is azimuthal modal number and $E_{r,z}(r, z)$ just slowly changes along the coordinate r ($\partial E_{r,z} / \partial r \approx 0$). This makes it possible to find each of the factors in Eq. (1) independently. In particular, in a VCSEL laser - which can be treated as a set of constant layers (perpendicular to the z axis (Fig. 1)), each of which is a collection of homogeneous cylinders - solutions in each such homogeneous region can be found analytically and then matched at borders using the continuity of the electric field and its derivative.

2.2. Fourier's Admittance Method

The Fourier's Admittance Method [2] is an example of a vector method. In this method, the electric field is expanded as a series of exponential plane-wave functions:

$$E(x, y, z) = \sum_{n=-\infty}^{\infty} c_n(z) \exp(ig_x x + ig_y y) \quad (2)$$

where g_n are successive reciprocal-lattice vectors of periodically repeated computational area. The above expansion is exact for the infinite number of components. However, in reality we are limited to using a finite number of functions. The actual number of considered series elements - hereafter referred to as N - should be chosen with consideration of the required accuracy of the calculations and the computation time constrains.

In the admittance method, expansion (2) is performed only laterally. In the vertical direction, the structure is divided into uniform layers. In each of layer a separate solution is obtained and then the results are combined at the layer boundaries using an admittance transfer algorithm [2].

2.3. Bessel's Admittance Method

Bessel's Admittance Method [3] is similar to the Fourier model. The difference is that instead of the expansion in the plane wave basis (Eq. (2)), the field is expanded into a Fourier-Bessel series of cylindrical waves:

$$E(r, \varphi, z) = \exp(iL\varphi) \sum_{n=1}^{\infty} c_n(z) J_L(\alpha_n r) \quad (3)$$

where J_L is the Bessel function of the first kind and its order L corresponds to the azimuthal mode in the EFM method. The parameter α_n is the n -th zero of the function J_L .

3. COMPARATIVE ANALYSIS OF METHODS

Our simulations were performed using the three computational methods described in section 2. We compared these methods by computing the dependence of the wavelength and the photon lifetime on the size of oxide aperture a .

3.1. Tested structure

The structure analyzed in this paper is a regular VCSEL structure. It consists of arsenide materials epitaxially grown on the gallium arsenide (GaAs) substrate. The active region is composed of three GaAs quantum wells separated by $\text{Al}_{0.3}\text{Ga}_{0.7}\text{As}$ barriers. The $1\frac{1}{2}$ -wavelength resonant cavity is surrounded by Bragg's quarter-wave mirrors (Distributed Bragg Reflectors (DBR)) made of $\text{Al}_{0.2}\text{Ga}_{0.8}\text{As}$ / $\text{Al}_{0.9}\text{Ga}_{0.1}\text{As}$. On the bottom there are 33 pairs of DBRs and on the top there are 25 pairs. In one of the simulated structures, there is a smooth transition between the layers made of $\text{Al}_{0.2}\text{Ga}_{0.8}\text{As}$ and $\text{Al}_{0.9}\text{Ga}_{0.1}\text{As}$. In this case the Al content changes gradually from 0.2 to 0.9. In the second structure, the transition layer is approximated by a single solid $\text{Al}_{0.55}\text{Ga}_{0.45}\text{As}$ material. This approximation allows to considerably simplify the calculations.

The schematic diagram of the structure described above is shown in Fig. 1. The symbols used in the figure are consistent with the rest of this paper, and are as follows: a – diameter of electrical aperture, x – aperture position along the active area, where $x = 1$ means the position in the standing wave antinode, and $x = 0$ indicates the position in the node.

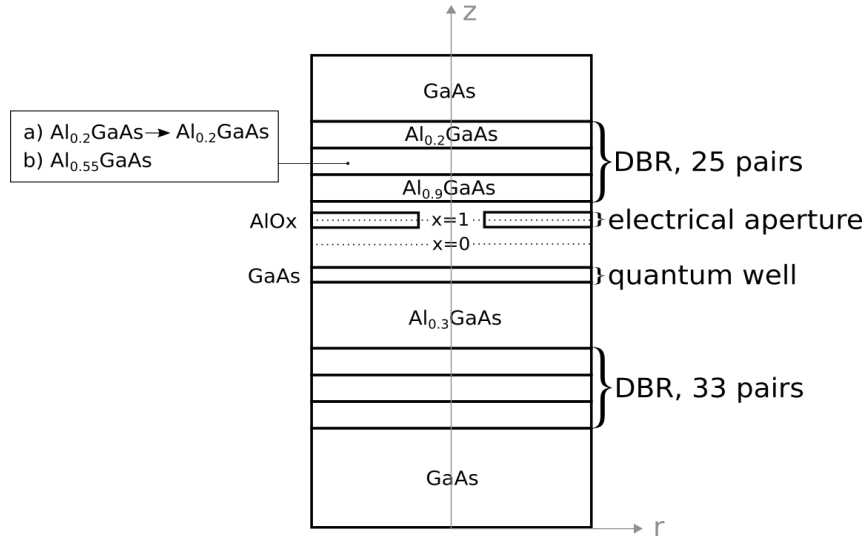


Fig. 1. Schematic diagram of the analyzed structure; the material compositions are shown for the first (a) and the second (b) analyzed structure; x is the position of the oxidation layer ($x = 0$ – standing wave node, $x = 1$ – standing wave antinode)

3.2. The comparison of methods

In the basic structure there is an intentional smooth molar composition transition between the DBR layers. As the first step of our analysis, we checked how replacing this smooth transition by one intermediate layer impacts the optical calculations result. For this purpose, we computed the dependence of resonant wavelength and photon lifetime on the aperture diameter for both the exact and approximated structures, using the EFM scalar method. As seen in Fig. 2, this approximation causes a slight change in the resonant wavelength for the fundamental mode, however the photon lifetime is systematically shifted by approximately 30%. This is due to the fact that the smooth layer transition, as in the structure (a), results in the lower DBRs reflectivity than in the structure (b). Fortunately, the photon lifetime difference between both structures remains constant and, hence, the results obtained for the approximate structure can be easily adjusted by scaling by a constant factor.

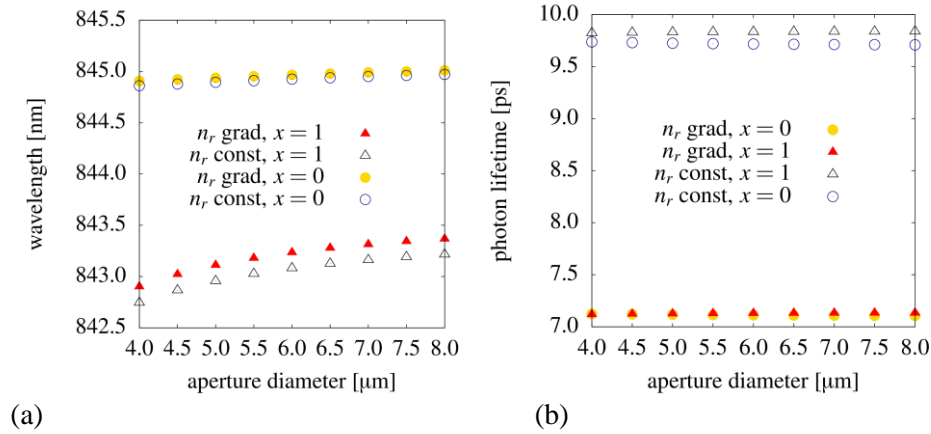


Fig. 2. The resonant wavelength (a) and the photon lifetime (b) as a function of the aperture diameter in the structures with constant (const) and gradually changing (grad) refractive index, n_r

Because of the above findings, further calculations were made for this second structure. We have compared the resonant wavelength and the photon lifetime on the aperture diameter obtained with different computational methods (Fig. 3). It can be seen that the scalar method differs greatly from the vector methods: the difference in the wavelengths obtained is around 2 nm. For comparison, the wavelength difference for the Bessel and Fourier methods is of the order of

hundredths of nm (Fig. 3a). A similar relationship can be observed for the photon lifetime. The difference between both vector methods is approximately 0.1 ps, while the values obtained by the EFM method deviate by about 1.0 ps (Fig. 3b). This is due to the approximation used in the scalar method (Eq. 1), which causes a systematic error to occur.

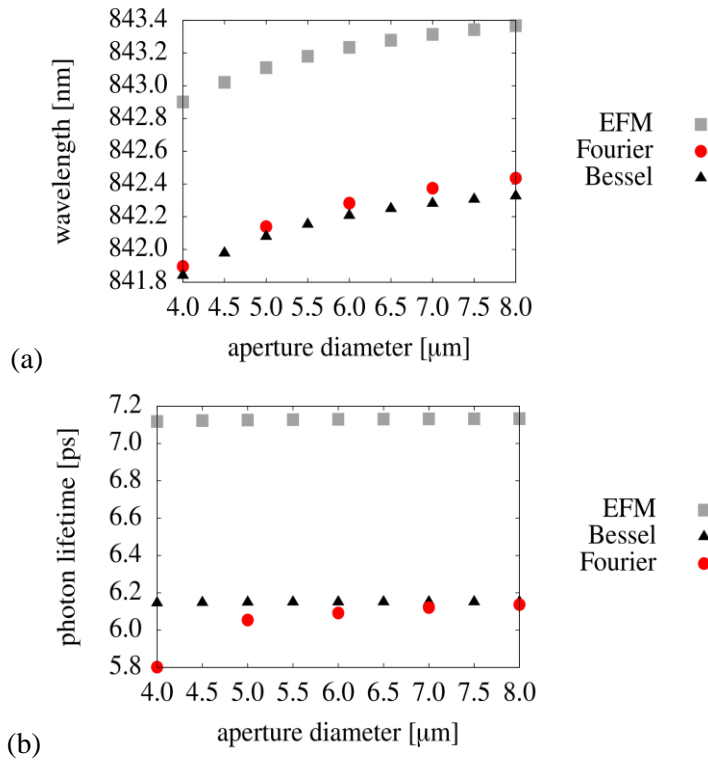


Fig. 3. The resonant wavelength (a) and the photon lifetime (b) as a function of the aperture diameter with $x = 1$

3.3. Convergence of the vector methods

Vector methods require the declaration of the N number of coefficients that will be used for a truncated Fourier or Fourier-Bessel series expansion. We investigated the influence of this parameter on the accuracy of our results. In the case of the Fourier model (Fig. 4), a shift in values can be observed, both in the wavelength and in photon lifetime. From $N = 20$ a stabilization can be seen. For the Bessel method (Fig. 5a), there is a 0.2 nm shift in the computed

wavelengths for $N < 10$. In the same compartment, a difference of 0.015 ps can be observed in the photon lifetime Fig. 5b). These shifts decrease in the range of $10 < N < 15$, while the stabilization is reached for $N \geq 15$.

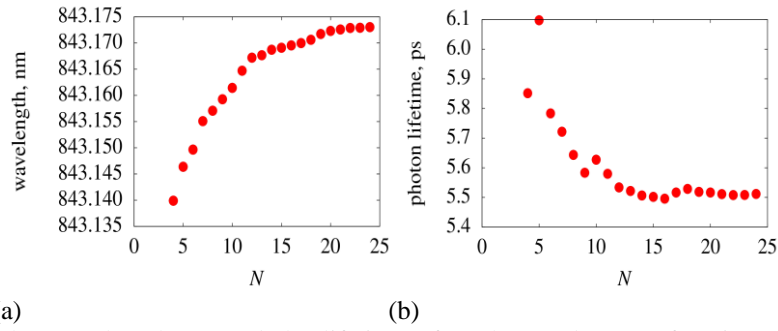


Fig. 4. The wavelength (a) and the lifetime of a photon (b) as a function of waves quantity with $x = 0.5$, $a = 4 \mu\text{m}$, Fourier method.

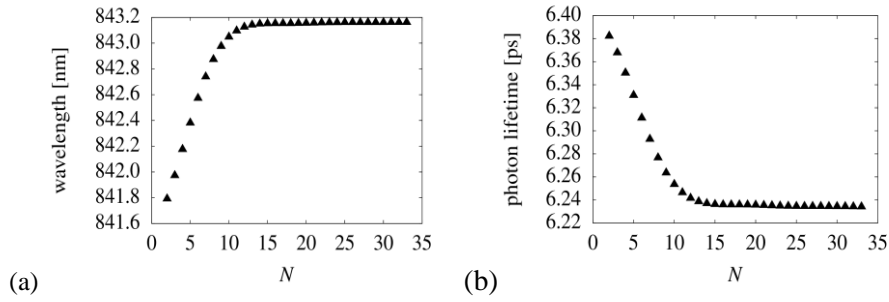


Fig. 5. The wavelength (a) and the lifetime of a photon (b) as a function of waves quantity with $x = 0.5$, $a = 4 \mu\text{m}$, Bessel method

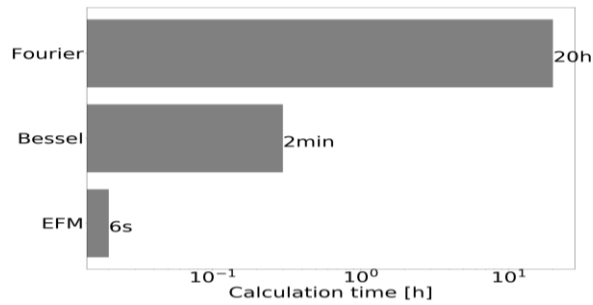


Fig. 6. The average calculation time for calculation methods

4. SUMMARY

This paper presents the results of a computer simulation for a VCSEL arsenide laser. The analysis consists of three parts. The first is dedicated to comparison of a structure in which there are layers with gradual refractive index change and for a structure in which these layers have been replaced by a solid material with a constant refractive index. The wavelength difference between these two structures is of the order of one tenth of a nanometer, while the calculation time for the structure with the gradual refractive index is several times longer than for the single-layer structure. For this reason, the calculations used to compare the models, which is the second objective of the paper, were performed for the second case.

Our calculations have shown that the scalar method differs greatly from vector methods. The difference in the resonant wavelengths between these models is much greater than the difference between the results obtained by both vector methods. A similar dependence can be observed in the case of differences in photon lifetime. The difference between the results obtained by the vector methods is much lower than the difference between them and the scalar EFM method. This is due to the approximation used in the EFM method. If it comes to the comparison of two vector methods, it can be seen that the Bessel's Admittance Method allows to obtain similar qualitatively and quantitatively results in a slightly shorter time. The average time of calculations for Fourier Method is 20 hours while the average time of calculations for Bessel model is 2 minutes.

The above analysis has shown that vector methods are more accurate than the scalar one. However, the accuracy of the latter ones depend on the number of considered coefficients. Our results show that their convergence can be assumed for $N \geq 20$ for the Fourier method and for $N \geq 15$ in the Bessel model. Fig. 6 shows the average computation times of the EFM scalar method and vector methods with the values of N as given above. The calculation time for the Fourier method is several times higher than for the other methods. The quickest is the scalar method, at the expense of accuracy.

Based on the analysis, it can be concluded that in the semiconductor structures modelling, it is worth using vector methods that give much more accurate results.

The paper was created within the project NCN 2015/19/B/ST7/00562: *Modelling novel VCSEL structures manufactured using intra-cavity selective planar oxidation for a high-power single-mode emission*. The work uses the results of POIG.01.03.01-00-159 InTechFun project implemented in the years 2009-2014 and was created during the period of its durability.

REFERENCES

- [1] Wenzel H., Wünsche H.-J. 1997. The effective frequency method in the analysis of vertical-cavity surface-emitting lasers. *IEEE J. Quantum Electron.* 33: 1156-1162.
- [2] Dems M., Kotynski R., Panajotov K. 2005. Plane-Wave Admittance Method – a Novel Approach for Determining the Electromagnetic Modes in Photonic Structures. *Opt. Express* 13: 3196-3207.
- [3] Dems M., Czyszanowski T., Panajotov K. 2006. Plane-Wave and Cylindrical-Wave Admittance Method for Simulation of Classical and Photonic-Crystal-Based VCSEls. *Proc.SPIE* 6182: 618219.
- [4] Nakwaski W. 2008. Principles of VCSEL designing. *Opto-electronics review* 16: 18-26.
- [5] Czyszanowski T., Nakwaski W. 2006. Usability limits of the scalar effective frequency method used to determine modes distributions in oxide-confined vertical-cavity surface-emitting diode lasers. *J. Phys. D: Appl. Phys.* 39: 30-35.
- [6] Bienstman P., Baets R., Vukusic J., Larsson A., Noble M. J., Brunner M., Gulden K., Debernardi P., Fratta L., Bava G. P., Wenzel H., Klein B., Conradi O., Pregla R. 2001. Comparison of Optical VCSEL Models on the Simulation of Oxide-Confined Devices. *IEEE J. Quantum Electron.* 37: 1618-1631.
- [7] Hadley G.R., Warren M.E., Choquette K.D., Scott J.W., Corzine S.W. 1996. Comprehensive Numerical Modeling of Vertical- Cavity Surface-Emitting Lasers. *IEEE J. Quantum Electron.* 32: 607-616.

PORÓWNANIE METOD SYMULACJI WŁAŚCIWOŚCI OPTYCZNYCH LASERÓW VCSEL

Streszczenie

W niniejszej pracy przedstawiono wyniki obliczeń propagacji emitowanej fali elektromagnetycznej (jej długości i czasu życia fotonów) dla arsenkowego lasera typu VCSEL. Celem pracy jest przedstawienie różnic płynących z zastosowania skalarnych i wektorowych metod obliczeniowych. Omówione wyniki pokazują, iż metody wektorowe są dużo dokładniejsze od metody

skalarnej, ale jednocześnie bardziej czasochłonne. Obliczenia przeprowadzono dla struktur różniących się wartością średnicy apertury oraz jej położeniem wzdłuż wnęki rezonansowej. Ponadto metodą skalarną wykonano obliczenia dla struktury, w której występują warstwy o gradientowo zmieniającym się współczynniku załamania, oraz dla struktury, w której warstwy te zastąpiono warstwą pośrednią o stałym współczynniku załamania. Celem pracy jest również pokazanie różnic w wynikach otrzymanych dla powyższych przypadków.

ISSN 1505-1013
e-ISSN 2449-982X
<http://cybra.lodz.pl/publication/3923>